

45 **Abstract**

46 ~~Understanding~~ Constraining dust models to understand and quantify the effect of dust upon climate
47 and ecosystems ~~needs-requires~~ comprehensive analyses of the physiochemical properties of dust-
48 emitting sediments in arid regions. Following previous studies in the Moroccan Sahara and Iceland,
49 hereHere, we analyse a diverse set of crusts and aeolian ripples (n=55) from various ~~dust-~~
50 ~~hotspots~~ potential dust-emitting basins within the Mojave Desert, California, USA. ~~We with~~ focus on
51 the characterization ~~on-of~~ their particle size distribution (PSD), mineralogy, aggregation/cohesion
52 state and ~~iron-Fe~~ mode of occurrence ~~characterization~~. Our results showed differences in fully and
53 minimally dispersed PSDs, with crusts average median diameters (92 and 37 μm , respectively)
54 compared to aeolian ripples (226 and 213 μm , respectively). Mineralogical analyses unveiled strong
55 variations between crusts and ripples, with crusts being enriched in phyllosilicates (24 vs 7.8 %),
56 carbonates (6.6 vs 1.1 %), Na-salts (7.3 vs 1.1 %) and zeolites (1.2 and 0.12 %), ~~while-and~~ ripples being
57 enriched in feldspars (48 vs 37 %), quartz (32 vs 16 %), and gypsum (4.7 vs 3.1 %). The size fractions
58 from crust sediments display a homogeneous mineralogy, while those of aeolian ripples are more
59 heterogeneous one, mostly due to their different particle aggregation. Bulk Fe content analyses
60 indicate higher concentrations in crusts (3.0 ± 1.3 wt %) compared to ripples (1.9 ± 1.1 wt %), with similar
61 ~~Fe-speciation~~ proportions in their Fe mode of occurrence; nano Fe-oxides/readily exchangeable Fe
62 represent ~ 1.6 %, hematite/goethite ~ 15 %, magnetite/maghemite ~ 2.0 % and structural Fe in silicates
63 ~ 80 % of the total Fe. We identified segregation patterns in PSD and mineralogy differences in Na-salts
64 content within the Mojave basins, ~~influenced by~~ that can be explained by sediment transportation
65 dynamics and precipitates due to groundwater table fluctuations described in previous studies in the
66 region. Mojave Desert crusts show similarities with previously sampled crusts in the Moroccan Sahara
67 for PSD and readily exchangeable Fe, yet exhibit substantial differences in mineralogical composition,
68 which ~~she~~ ould significantly influence the emitted dust particles characteristics.

69

70 **Keywords:** Arid regions, dust sources, desert dust, dust-emitting sediment formation model, dust
71 mineralogy.

72

73 1. Introduction

74 Desert dust produced by wind erosion of arid and semi-arid surfaces has ~~important~~significant effects
75 on climate and ecosystems (Weaver et al., 2002; Goudie & Middleton, 2006; Sullivan et al., 2007;
76 Crumeyrolle et al., 2008; De Longeville et al., 2010; Karanasiou et al., 2012; Pérez García-Pando et al.,
77 2014; among others). Dust affects the energy and water cycles through its absorption and scattering
78 of both shortwave (SW) and longwave (LW) radiation (Perez et al., 2006; Miller et al., 2014), and exerts
79 influence on cloud formation, precipitation patterns, and the associated indirect radiative forcing by
80 serving as nuclei for liquid and ice clouds (e.g. Harrison et al., 2019). Dust also undergoes
81 heterogeneous chemical reactions in the atmosphere that enhance their hygroscopicity and modify
82 their optical properties (Bauer et al., 2005), and when deposited into ocean waters, its bioavailable
83 iron content acts as a catalyst for photosynthesis by ocean phytoplankton, thereby increasing carbon
84 dioxide uptake and influencing the global carbon cycle (Jickells et al., 2005).

85 Dust primarily originates from arid inland basins, which include various sedimentary environments
86 such as aeolian deposits, endorheic depressions, and fluvial- and alluvial-dominated systems (Bullard
87 et al., 2011). Wind typically mobilizes loose sand from adjacent ripples or dunes, which then erodes
88 more consolidated surfaces, typically paved sediments and crusts, to release dust (Stout and Lee,
89 2003; Shao et al., 2011). Atmospheric dust emission models have improved by identifying preferential
90 dust sources using criteria like topography and hydrology (Ginoux et al., 2001). However, these models
91 still struggle with capturing small-scale variability partly due to the lack of relevant soil measurements
92 in arid regions, despite advancements in understanding the geomorphological and sedimentological
93 factors influencing dust emissions (Bullard et al., 2011). For instance, the particle size distribution
94 (PSD) and cohesion of the sediments affect saltation bombardment and aggregate disintegration
95 processes involved in dust emission (Shao et al., 1993).

96 Understanding the mineral composition of dust is also crucial for assessing its climate impact. Dust
97 contains various minerals such as quartz, clay minerals, feldspars, carbonates, salts, and iron oxides.
98 The climate effects of dust are influenced by these minerals' relative abundances, sizes, shapes, and
99 mixing states. For example, iron oxides control solar radiation absorption by dust (Formenti et al.,
100 2014; Engelbrecht et al., 2016; Di Biagio et al., 2019; Zubko et al., 2019), nano Fe oxides and easily
101 exchangeable Fe increase the fertilising effect of dust in ocean and terrestrial ecosystems
102 (Hettiarachchi et al., 2019; Baldo et al., 2020, Hettiarachchi et al., 2020), K-feldspar and quartz impact
103 ice nucleation in clouds (Atkinson et al., 2013; Harrison et al., 2019; Chatziparaschos et al., 2023), and
104 calcite influences acid reactions on dust surfaces (Paulot et al., 2016). The mineralogical composition
105 of dust can vary significantly across different regions due to geological and climatic factors (Claquin et
106 al., 1999; Journet et al., 2014). However, most models assume a globally uniform dust composition
107 due to limited global data on parent soil sources. Only a few models account for dust mineralogical
108 composition variations (e.g., Scanza et al., 2015; Perlwitz et al., 2015; Li et al., 2021; Gonçalves Ageitos
109 et al., 2023; Obiso et al., 2024) by using global soil type atlases and extrapolating from a limited
110 number of analyses (Claquin et al., 1999; Journet et al., 2014). These atlases rely on assumptions about
111 soil texture and color, often base their data on soil samples taken from depths deeper than those
112 relevant to wind erosion, and the method used to characterize particle size and associated mineralogy
113 fully breaks down natural soil aggregates.

114 Since 2022, the EMIT mission has been acquiring comprehensive measurements of surface
115 mineralogical composition for use in Earth System models (Green et al., 2020). EMIT employs imaging
116 spectroscopy across the visible to short wavelength infrared (VSWIR) spectral range from the
117 International Space Station to map the occurrence and estimate the abundance of ten key dust source
118 minerals. Additionally, EMIT has the potential to estimate surface soil texture. While identifying
119 dominant surface minerals has traditionally been a strength of spectrometers, quantifying these
120 minerals poses significant challenges. Factors such as mineral grain size and composition can affect
121 spectral absorptions, certain dominant materials like quartz and feldspar exhibit minimal absorption
122 features, and the presence of other materials can further complicate the analysis.

123 Overall, there is a notable lack of comprehensive measurements characterizing relevant properties of
124 surface sediments in dust source regions. This gap hampers our ability to evaluate and constrain
125 mineral abundance derived from reflectance spectroscopy and to improve dust emission modeling.
126 Addressing this issue, the FRontiers in dust minerAloGical coMposition and its Effects upoN climaTe
127 (FRAGMENT) project has, over recent years, conducted a series of coordinated and interdisciplinary
128 field campaigns across remote dust source regions. The project's objectives include enhancing the
129 understanding and quantification of dust-source properties, examining their relationship with emitted
130 dust characteristics, refining spaceborne spectroscopy retrievals of surface minerals (Green et al.,
131 2020, Clark et al., 2024), and improving the representation of dust mineralogy in Earth system models
132 (Perlwitz et al., 2015; Li et al., 2021; Gonçalves et al., 2023; Obiso et al., 2023). The FRAGMENT field
133 campaigns involved regional sediment sampling in several regions and detailed wind erosion and dust
134 emission measurements at selected sites. Studies stemming from these activities include those by
135 González-Romero et al. (2023), González-Flórez et al. (2022), and Panta et al. (2022), and González-
136 Romero et al. (2024). These campaigns have been executed in various geographic locations, such as
137 the Moroccan Sahara (2019), Iceland (2021), the Mojave Desert in the United States (2022), and
138 Jordan (2022). Through these efforts, the FRAGMENT project contributes to filling critical knowledge
139 gaps in dust-source characterization.

140 Following our previous studies in the Moroccan Sahara (González-Romero et al. 2023) and Iceland
141 González-Romero et al. (2024), Both dust emission processes and climate perturbations by dust
142 depend fundamentally upon the physical and chemical properties of the dust-emitting sediments from
143 different sources. For instance, the particle size distribution (PSD) and cohesion of the sediments
144 affect saltation bombardment and aggregate disintegration processes involved in dust emission (Shao
145 et al., 1993). The content of iron oxides (mainly hematite and goethite) determines the absorption of
146 solar radiation by dust (Formenti et al., 2014; Engelbrecht et al., 2016; Di Biagio et al., 2019; Zubko et
147 al., 2019), that of nano-Fe oxides and easily exchangeable Fe increase the fertilising effect of dust in
148 ocean and terrestrial ecosystems (Hettiarachchi et al., 2019; Baldo et al., 2020, Hettiarachchi et al.,
149 2020), and that of K-feldspar and quartz increases the ice nucleation efficiency of dust (Atkinson et al.,
150 2013; Harrison et al., 2019; Chatziparaschos et al., 2023). Overall, a notable gap exists in our
151 understanding of the properties of dust-emitting sediments, including particle size distribution,
152 cohesion, mineral composition, and Fe mode of occurrence from different dust sources. This
153 deficiency hinders the development of precise model simulations necessary for accurately assessing
154 the emission and transport of dust and its associated climate and environmental impacts (Raupach et
155 al., 1993; Laurent et al., 2008; Perlwitz et al., 2015; Kok et al., 2021).

156 This study focuses on the characterization of dust-emitting sediments collected from the Mojave
157 Desert in 2022. The Mojave Desert is a closed-basin wedge-shaped region located in the southwestern
158 United States, between California and Nevada. The region is surrounded by mountain ranges and
159 traversed by the Mojave river and other intermittent rivers for over 200 km from the San Bernardino
160 mountains to the east (Dibblee, 1967, Reheis et al., 2012). Despite its limited global importance (dust
161 emission from North America represents only ~3 % of the global dust emission; Kok et al., 2021), the
162 Mojave Desert is an important regional dust source (Ginoux et al., 2012), with most emission occurring
163 in the playa lakes and alluvium deposits near playa lakes (Reheis & Kihl, 1995; Reheis et al. 2009, Urban
164 et al., 2018). Reynolds et al. (2009) observed 71 days with dust plumes during 37 months of camera
165 recording at the Franklin Lake playa. According to remote sensing data (MODIS) from years
166 2000-2005 over the Mojave Desert, aerosol optical depth (AOD) is higher in spring and summer and
167 reaches a minimum in winter (Frank et al., 2007). However, from November to May, eastward flows
168 of the jet-stream affect the Mojave Desert, which, in combination with topography, favour the
169 development of northerly winds that can lead to dust emission (Urban et al., 2009). Up to 65 %
170 of emission in the Mojave Desert is estimated to be due to natural factors, whereas the remaining
171 35 % is caused by anthropogenic activities, including off-road recreation practices, mine operations,
172 and military training and livestock grazing, while livestock grazing has reduced vegetation cover
173 (Frank et al., 2007). The AOD in this region is also affected by dust transported from other regions
174 (Tong et al., 2012) and pollution transported from the Los Angeles Basin (Frank et al., 2007, Urban et
175 al., 2009). In the Mojave Desert, Reynolds et al. (2009) noted an association between wet periods and
176 dust emission, directly related to the generation of new thin crusts and salt crust removal.

177 The Mojave Desert includes several significant playa lakes, such as Rogers and Rosemond, Owens Lake,
178 Death-Valley-Badwater, Panamint Valley, Bristol, Cadiz and Danby, Searles Lake, Soda Lake, and
179 Mesquite Lake, among others (Reheis & Kihl, 1995; Reheis, 1997; Potter and Coppernoll-Houston,
180 2019). Reynolds et al. (2007 and 2009) distinguished between two types of playa lakes: wet playas
181 influenced by groundwater, and dry playas, unaffected by groundwater, though both can experience
182 surface-water runoff. Goudie (2018) further delineated wet playas as having a groundwater table
183 within 5 m of the surface, while dry playas have a groundwater table deeper than 5 m. Additionally,
184 Goudie (2018), Buck et al. (2011), Nield et al. (2015) and Nield et al. (2016) observed that the
185 interaction between salt minerals and the groundwater table on wet playas lead to the formation of
186 fluffy surfaces through salt reworking by water during evapotranspiration.

187 In the Mojave Desert, three different aridisols are present in the Rand mountains
188 alluvial fan, corresponding to Xerillic soils or Aridisols according to Eghbal & Southard (1993), typical
189 from in arid and semi-arid regions, with low organic matter content and low structures. The
190 uppermost layer of those aridisols, ranging from 0 to 1 cm in depth exhibited a texture of 15-30%
191 gravel, 69-74 % sand and 10-11 % clay. Reheis et al. (1995) described soils (<2 mm) primarily composed
192 of silt (30-70 %) and clay (20-45 %). The mineralogy of those samples was dominated by quartz,
193 feldspars, amphiboles, and clay minerals, including smectite, mica and kaolinite (Eghbal & Southard,
194 1993). The Cronese Lakes and Soda Lake playas are documented to contain salt precipitates, but
195 mineralogy is not specified. Mesquite Lake playa is noted for its gypsum deposits (Reynolds et al.,
196 2009). At Franklin Lake playa, surfaces are characterized by silt-clay size particles (Goldstein et al.,
197 2017) with mineralogical descriptions provided by Reynolds et al. (2009) indicating fluffy surfaces
198 comprised of halite, thenardite, trona, burkeite, calcite, illite, smectite, and kaolinite. Similar
199 mineralogical results are described at Soda Lake by Reheis et al. (2009), with a higher proportion of

200 Na-salts, quartz, gypsum and carbonates. Furthermore, Goldstein et al. (2017) identified a diverse
201 array of minerals at Franklin Lake playa, including clays, zeolites, plagioclase, K-feldspar, quartz,
202 calcite, dolomite and salt minerals such as trona, halite, burkeite and thenardite.

203 This study characterises the particle size distribution, mineralogy and modes of ~~mode of~~
204 occurrence of Fe of selected potential dust-emitting sediments surfaces ~~in from~~ the
205 Mojave Desert, where a sediment sampling was carried out in 2022 around the Soda, Mesquite,
206 Ivanpah, Coyote and Cronese playa lakes, in the context of the FRontiers in dust minerAloGical
207 coMposition and its Effects upoN climate (FRAGMENT) project. In addition, the mineralogy of different
208 size fractions is analysed, based on a sieving protocol that minimally disturbs sediments. We further
209 discuss the potential effect of sedimentary transport on the particle size and mineralogy across the
210 sampled basins building upon previous studies in the literature. Finally, our results are broadly
211 compared with current EMIT mission results standard (semi-quantitative) products, and with those
212 obtained using similar protocols from previous campaigns carried out in previous FRAGMENT
213 campaigns in other regions in the Moroccan Sahara in 2019 (González-Romero et al., 2023; González-
214 Romero et al., 2024) and Iceland in 2021 (González-Romero et al., 2024).

215 2. Methodology

216 2.1 Study area

217 The Mojave Desert, located between California and Nevada, has a diverse geological history spanning
218 from the Cambrian and Precambrian eras to the Holocene (Figure 1). This geological complexity
219 encompasses volcanic, plutonic, metamorphic, and sedimentary units (Jennings et al., 1962; Miller et
220 al., 2014). In areas once submerged during the last glacial maximum (LGM), we now find ephemeral
221 playa lakes that have existed for thousands of years since the LGM, offering a glimpse into the region's
222 dynamic past (Miller et al., 2018). These playa lakes together with alluvial fans, floodplains and other
223 features are, surrounded by a variety of source rocks, exhibit diverse particle sizes and compositions
224 and can potentially emit dust under favourable wind conditions.

225 The regional distribution of the annual Frequency of Occurrence (FoO) of dust events, with dust optical
226 depth exceeding 0.1, derived from MODIS Deep Blue C6.1 Level 2 data following the methodology of
227 Ginoux et al. (2012), is illustrated in Figure 2. The FoO provides an overall estimate of dust emission
228 frequency above a certain threshold at a resolution of 0.1° by 0.1° over the region. Sediment samples
229 were collected from various locations within the Mojave Desert region, including areas with relatively
230 high FoO (see locations in Figures 1 and 2). Among these locations is Soda Lake and its surroundings,
231 near Baker, CA, which is linked to Silver Lake to the north and is surrounded by igneous, volcanic, and
232 carbonate rocks, as well as dune fields to the south (Figure 1). The area is influenced by aeolian,
233 alluvial, and fluvial processes and experiences annual precipitation of 80-100 mm (Urban et al., 2018).
234 This ephemeral lake contains salts resulting from the evaporation of groundwater sourced from an
235 aquifer nestled in the Zzyzx Mountains (Honke et al., 2019). Dust emissions are a recurrent
236 phenomenon, originating from fine sediments accumulated in the lake's central areas during sporadic
237 floodings, from the white evaporite surfaces in the lake, and from the alluvial deposits to the south of
238 the playa lake (Urban et al., 2018). According to the FoO, the areas with higher dust emissions are the
239 southern part of the lake and the alluvial deposits to the southwest, extending up to Afton Canyon. The

240 such examples is Soda Lake, located near Baker, CA, which undergoes influences from aeolian, alluvial
241 and fluvial processes, and experiences an annual precipitation of 80-100mm (Urban et al., 2018). This
242 ephemeral lake contains salts resulting from the evaporation of groundwater sourced from an aquifer
243 nestled in the Zzyzx mountains (Honke et al., 2019). Dust emissions are a recurrent phenomenon,
244 primarily originated from fine sediments accumulated in the lake's central areas and the alluvium
245 deposits around the playa lakes during sporadic floodings, as well as from the white evaporite surfaces
246 found in the lake (Urban et al., 2018).

247
248 Samples of dust-emitting sediments were collected from various sites within the Mojave Desert
249 region. Among these sites is Soda Lake, situated near the Zzyzx complex (the California State University
250 Desert Studies Centre), which is linked to Silver Lake to the north, and surrounded by igneous, volcanic
251 and carbonate rocks, as well as dune fields to the south (Figure 1). Samples were also collected from
252 the Cronese lakes, Mesquite Lake, Ivanpah Lake and Coyote Lake (Figure 1), which lie in areas with
253 significant FoO signals (Figure 2) and have been documented as dust sources in Reheis & Kihl (1995)
254 and Reheis et al. (2009). The Cronese lakes are adjacent to the Soda Lake area to the west, lie the
255 Cronese lakes, positioned to the northwest and sharing a similar geologic context (Figures 1 and 2).
256 Mesquite Lake, located on the border between California and Nevada, is encircled by carbonate and
257 igneous rocks, mirroring the geological setting of the nearby Ivanpah Lake. (Figure 1). Notably,
258 Mesquite Lake playa is the only playa affected by a gypsum mine pit, as documented by Reynolds et
259 al. (2009). Further contributing to the diversity of the region's geological makeup is Coyote Lake,
260 flanked by Miocene and Pleistocene sediments. (Figure 1). These playa lakes, characterized as
261 endorheic ephemeral lakes, receive in some cases groundwater inputs in some cases, enriching the
262 lakes with salts that subsequently precipitate on the surfaces of their central regions (Whitney et al.,
263 2015; Urban et al., 2018).

264 Other areas with relatively high FoO not sampled in our study include the Ashford Junction alluvial
265 deposits and the Fort Irwin area, where the northern valley, including Nelson Lake, may be more prone
266 to dust emission due to significant anthropogenic disturbance. It is important to note that the FoO
267 may tend to highlight areas such as playas and their surroundings, where in some cases the most dust
268 per unit area could be produced (Floyd and Gill, 2011; Baddock et al., 2016). However, some alluvial
269 regions with lower emission rates not surpassing the FoO threshold may produce more dust overall
270 due to their greater areal extent (Reheis and Kihl, 1995; Baddock et al., 2016). Additionally, many other
271 types of dust-producing surfaces active in the Mojave Desert, such as gravel roads, agricultural lands,
272 and recreational off-road tracks, are rarely observed by satellite retrievals (Urban et al., 2018).

273 Figure 2 illustrates the regional distribution of the annual Frequency of Occurrence (FoO) of dust
274 events with dust optical depth exceeding 0.1, as derived from MODIS Deep Blue C6.1 Level 2 data.
275 Notably, the map highlights active dust hotspots at Soda, Cronese, and Coyote lakes, as well as at
276 Ivanpah and Mesquite lakes, alongside other notable areas (Figure 2).

277 The new EMIT sensor onboard the International Space Station offers a glimpse of the mineralogical
278 diversity in the Mojave Desert (Green et al., 2020). Figure 3 displays standard Tetracorder RGB color
279 composite semi-quantitative products for EMIT. Tetracorder is a software system that employs a set
280 of algorithms within an expert system decision-making framework to identify and map compounds
281 (Clark, 2024; Clark et al., 2024). Figure 3 shows a true color image, along with standard products for

282 Fe²⁺ and Fe³⁺ bearing mineral electronic absorptions (including hematite and goethite) in the visible
283 to very-near infrared spectral range. It also displays standard products for the EMIT-targeted minerals,
284 excluding hematite and goethite: calcite, chlorite/serpentine, dolomite, gypsum, illite/muscovite,
285 kaolinite-dioctahedral group, montmorillonite group, and vermiculite. These products highlight areas
286 where the presence of each mineral or component is significant, measured in terms of band depth*fit,
287 where the fit represents the least squares correlation coefficient from a feature fit of observed and
288 reference library spectra. These analyses reveal the widespread presence of phyllosilicates such as
289 kaolinite, smectite, montmorillonite, and illite across the area. The northeastern sector, particularly
290 around Mesquite Lake, exhibits notable concentrations of carbonates and gypsum. Additionally,
291 goethite and hematite are detected, with a more pronounced presence of goethite in the northern
292 portion and hematite in the southern part of the region. The detection of mixtures of Fe²⁺ and Fe³⁺
293 within various minerals enriches our understanding of the region's mineralogical diversity.

294 Quantitative surface mineralogy (mineral mass abundances of the 10 EMIT-targeted minerals) and soil
295 texture products are currently being developed by the EMIT team for use in Earth System Models.
296 Their publication and evaluation will be the focus of forthcoming publications. Thus, it is beyond the
297 scope of this study to perform a detailed quantitative comparison between our analyses and
298 comparable EMIT products. However, in the results section, we broadly compare these standard
299 products with the results of our in-situ analyses. Preliminary mineralogical identification maps derived
300 from the Earth Surface Mineral Dust Source Investigation (EMIT) imaging spectrometer onboard of
301 the International Space Station (Green et al., 2020) based on the mineral mapping refinement
302 technique developed by Clark et al. (2023) known as Tetracorder, offer a glimpse into the rich
303 mineralogical tapestry of the region (Figure 3). These analyses reveal the widespread presence of
304 phyllosilicates such as kaolinite, smectite, montmorillonite, and illite across the area, with the
305 northeastern sector, particularly around Mesquite Lake, exhibiting notable concentrations of
306 carbonates and gypsum. Additionally, goethite and hematite are detected, with a more pronounced
307 presence of goethite in the northern portion and of hematite in the southern part of the region. Of
308 significance is the detection of mixtures of Fe²⁺ and Fe³⁺ within various minerals, enriching our
309 understanding of the region's mineralogical diversity.

311 **2.2 Sampling**

312 Representative surfaces of dust-emitting sediments were sampled in May 2022 in the above playa
313 lakes, with depths of up to 3 cm, using a 5 cm² inox shovel. Samples were stored in a plastic bag,
314 labelled, and documented with photographs, descriptions, and coordinates, and transported to the
315 laboratories for subsequent analyses. The type of samples considered are crusts (semi-cohesive fine
316 sediments accumulated during floodings in depressions) and ripples (aeolian ripples that are built up
317 under favourable winds and supply sand for saltation) (Figure 4). A total of 55 surface sediments and
318 ripples (32 from Soda Lake, 9 from Mesquite Lake, 1 from Ivanpah Lake, 11 from the Cronese Lakes,
319 and 2 from Coyote Lake) were sampled for laboratory analysis. Once in the laboratory, the samples
320 were dried for 24-48 h at 40-50 °C, sieved to pass through a 2 mm mesh.

321 Our rationale for selecting crusts and ripples is two-fold. On the one side, dust emission is primarily
322 driven by two mechanisms: saltation bombardment and aggregate disintegration. In saltation

323 bombardment, dust is ejected from soil aggregates (typically crusts and paved sediments rich in clay
324 and silt particles) when impacted by saltating sand particles. In aggregate disintegration, dust is
325 released from saltating soil aggregates (Shao et al., 1993; Alfaro et al., 1997; Shao, 2001). By
326 characterizing the PSD (both dry and wet sieved) and mineralogy of ripples (concentrating sand
327 particles) and crusts (concentrating clay and silt particles), we provide comprehensive and valuable
328 information for developing and refining dust emission models. On the other side, in arid regions,
329 quartz and feldspar typically dominate sediment mass. However, current spaceborne hyperspectral
330 instruments (such as EMIT) cannot directly identify feldspar and quartz because their absorption
331 features lie outside the instrument's spectral range. This poses a significant challenge in quantifying
332 surface mineral abundances from remote spectroscopy. At all FRAGMENT sampling locations
333 (Morocco, Iceland, US-Mojave, and Jordan), we measured reflectance spectra using an ASD Fieldspec
334 3. By characterizing and contrasting ripples (with high quartz and feldspar content and larger particle
335 sizes) and crusts, we aim to provide information to enhance understanding and improve modeling
336 assumptions for estimating surface mineral abundances and soil texture from remote spectroscopy in
337 subsequent studies.

338 We acknowledge that the limited number of samples collected may not fully represent the potential
339 variability among crusts and ripples within the studied locations due to varying conditions (Buck et al.,
340 2011). However, our samples broadly represent the composition and particle size distributions (PSDs)
341 of this type of sediments in these areas, allowing for meaningful comparisons with sediments from
342 other locations.

343 Once in the laboratory, the samples were dried for 24-48 h at 40-50 °C, sieved to pass through a 2 mm
344 mesh, and separated into homogeneous sub-samples for subsequent analyses. A total of 55 surface
345 sediments and ripples (32 from Soda Lake, 9 from Mesquite Lake, 1 from Ivanpah Lake, 11 from the
346 Cronese Lakes, and 2 from Coyote Lake) were sampled in May 2022 for laboratory analysis.

347 **2.3 Analyses**

348 2.3.1 Particle size distribution

349 Particle size distributions (PSD) of bulk samples (<2 mm) were analysed as described in González-
350 Romero et al. (2023) for the evaluation of the aggregation state. First, we conducted a minimally
351 dispersed PSD (MDPSD) analysis, which minimizes the breaking of the aggregates that are
352 encountered in natural conditions. Second, we conducted a fully dispersed PSD (FDPSD) analysis,
353 which breaks the aggregates. Wet dispersion was done according to Sperazza et al., (2004), using
354 water and sodium hexametaphosphate dispersion for 24 h. Both PSDs (MDPSD and FDPSD) were
355 obtained by a laser diffractometer with the Malvern Mastersizer 2000 Hydro G and Scirocco for the
356 fully and minimally dispersed conditions, respectively. We note that under wet dispersion, at least
357 some salt minerals may dissolve.

358 In addition, we separated 20 selected samples from different sources, including 16 crusts and 4 aeolian
359 ripples, into different size ranges to understand how mineral composition changes with size. We used
360 a series of sieves with mesh sizes of 2 mm, 1 mm, 500 µm, 250 µm, 80 µm, 63 µm, 40 µm, and 20 µm.
361 The sieving process involved hand shaking the full column for 1 minute, followed by ultrasound

362 [sonication for 1 minute at the 500 \$\mu\text{m}\$, 80 \$\mu\text{m}\$, 40 \$\mu\text{m}\$, and 20 \$\mu\text{m}\$ size fractions. This method ensured](#)
363 [the effective separation of the size fractions for subsequent mineralogical analysis.](#)

364 2.3.2 Mineralogical composition

365 To quantify the different contents of crystalline minerals and amorphous components, X-Ray
366 Diffraction (XRD) coupled with a Rietveld quantitative method were used (Rietveld, 1969; Cheary and
367 Coelho, 1992; Young, 1995 and Topas, 2018). Adding a known amount of an internal standard material
368 allowed, via the Rietveld method, the quantification of a mixture of minerals and any non-crystalline
369 material in the mixture not included in the Rietveld method (De la Torre et al., 2001; Madsen, 2001,
370 Scarlett and Madsen, 2006; Machiels et al., 2010; Ibañez et al., 2013). For the analysis, a measured
371 amount of dry ground ~~ed~~ sample ~~is-was~~ mixed and dry ground ~~ed~~ again with 10-20 % of fluorite (CaF_2
372 powder, Merck), used here as an internal standard for quantitative purposes. The XRD patterns of the
373 samples were analysed by a Bruker D8 A25 Advanced Powder X-ray diffractometer operated at 40kV
374 and 40 mA with monochromatic $\text{Cu K}\alpha$ radiation ($\lambda=1,5405 \text{ \AA}$). This device uses a Bragg-Brentano
375 geometry and a sensitive detector LynxEye 1D. Diffractograms were recorded from 4 to 120° of 2θ
376 and steps of 0.015° in 1s and maintained rotation (15/min). For the clay identification, samples were
377 analysed using the oriented aggregate method by XRD, decanting clay fractions from samples and
378 smearing the slurries in glass slides. After, three treatments were applied including air drying (AO),
379 glycolation with ethylene glycol (AG) and heating at 550°C for 2h (AC) with its three different
380 diffractograms. Finally, the three diffractograms allows ~~us-~~ to corroborate the presence of Illite,
381 Chlorite, Palygorskite and Montmorillonite through Thorez (1976) and USGS Open File procedures.
382 Data collected were evaluated using the Bruker AXS DIFFRAC.EVA software package (Bruker AXS,
383 Karlsruhe, Germany, 2000) and the Rietveld analyses performed with TOPAS 4.2 program (Bruker AXS,
384 2003-2009). A Chebyshev function of level 5 was used to fit the background and abundances of
385 crystalline phases and amorphous phases were normalised to 100 wt %. Fits were evaluated by visual
386 comparison, the R_{wp} (R-weighted pattern), R_{exp} (R-expected), and Goodness of Fit (GOF).

387 2.3.3 Mode of occurrence of Fe

388 As XRD is not precise enough for Fe-oxide quantification, wet chemistry and sequential extractions of
389 Fe are needed for quantification of the [modes of Fe mode of occurrence occurrences of Fe](#) (González-
390 Romero et al., 2023; 2024). Samples were analysed with a two-step acid digestion for the total Fe (FeT)
391 content following the procedure by Querol et al. (1993, 1997). A reference material (NIST-1633b, coal
392 fly ash) was used for quality control in every batch. The sequential extraction presented in Shi et al.
393 (2009), Baldo et al. (2020) and González-Romero et al. (2024) ~~was-were~~ used to quantify readily
394 exchangeable Fe ions and nano Fe oxides (FeA), the amount of crystalline Fe oxides as goethite and
395 hematite (FeD), and ~~crystallised-crystalline~~ magnetite (FeM). For the 1st extraction, ~~a~~ 30 mg sample
396 ~~was-were~~ leached with 10 ml of an ascorbate solution (extractant solution) and shaken in dark
397 conditions for 24 h and filtered. Another 30 mg ~~was-were~~ leached with 10 ml of a dithionite solution
398 (extractant solution), shaken for 2 h in dark conditions and filtered for the 2nd extraction. The solid
399 residue was then leached again in 10 ml of an oxalate solution for 6 h in dark conditions and filtered
400 for the 3rd extraction. The extracted solution of each phase (FeT, FeA, FeD and FeM) was analysed to
401 quantify dissolved Fe by Inductively Coupled Plasma Atomic Emission Spectrometry (ICP-AES). FeA is
402 obtained with the 1st extraction, FeD is obtained subtracting from the 2nd extraction the amount of

403 Fe from the 1st extraction. Finally, the FeM is related to the 3rd extraction. At the end, the equivalent
404 to the Fe as structural Fe was obtained: $FeS = FeT - FeA - FeD - FeM$ which is included in other minerals
405 and amorphous phases. To test accuracy, 30 mg of Arizona Test Dust (ATD; ISO 12103-1, A1 Ultrafine
406 Test Dust; Powder Technology Inc.) was subjected to the same extraction procedure in every batch
407 and extraction.

408 The averaged Fe content of the reference material 1633b was $7.6 \pm 0.5 \%$ (certified 7.8%).
409 Furthermore, the average values of the sequential Fe extraction of the ATD reference material were
410 0.073 ± 0.012 , 0.47 ± 0.01 , and $0.042 \pm 0.002 \%$ for FeA, FeA+FeD and FeM, respectively, while the
411 certified contents are 0.067, 0.48, and 0.047 %, respectively.

412 3. Results

413 3.1. Particle size distribution

414 The PSD and ~~the~~ median particle diameter of fully and minimally disturbed samples are key
415 parameters ~~forte~~ understanding the cohesion and aggregation state of ~~the~~ sediments (González-
416 Romero et al., 2024). We note that in the case of the Mojave Desert, some basins are enriched in
417 salts, which can cause some artefacts in the FDPD. The dissolution of salts during wet dispersion for
418 bulk PSD analysis (<2 mm) can remove aggregating agents. as there can be removal of the aggregating
419 agents by dissolution during the wet dispersion for the PSD analysis. These salt cementation of the
420 crusts might ~~yield very reduced dust emissions~~ reduce the dust emission potential of the surface.

421 The average PSDs of crusts across different basins exhibit remarkable similarity, yet disparities
422 between FDPDs and MDPSDs are pronounced, indicating varying degrees of particle cohesion and
423 aggregation at Cronese, Mesquite, Ivanpah and Coyote lakes. In ~~these~~ ~~thesese~~ locations, FDPDs
424 feature a dominant mode at 8-10 μm alongside a coarser mode at 100 μm , while MDPSDs are
425 characterized by a dominant coarser mode (Figure 5). In contrast, Soda Lake crusts, exhibit similarity
426 between FDPDs and MDPSDs. ~~When comparing a~~ Averaged FDPDs and MDPSDs of aeolian ripples
427 from the Mojave Desert, ~~they~~ are found to be similar, typically featuring a major size mode between
428 100-300 μm . However, distinctions arise when analysing specific lakes. Aeolian ripples from Soda,
429 Cronese, and Coyote lakes showcase a dominant coarse mode at 200-300 μm , while whereas those
430 from Mesquite Lake show a dominant mode at a finer scale, approximately at 100 μm (Figure 5).

431 The crusts' mean of all median ~~(mean median)~~ particle diameters (mean median) in the ~~aevaluated~~
432 analyzed Mojave Desert dust source sedimentss reveal a coarser MDPSD compared to FDPD, with
433 values of 92 and 37 μm , respectively. In contrast, the mean median particle diameter is similar for
434 aeolian ripples (226 and 213 μm , respectively) (Table S1). Analysing specific locations, the mean
435 median particle diameter from the MDPSD of crusts varies, with the finest crust observed at Ivanpah
436 Lake (35 μm) and the coarsest at Mesquite Lake (141 μm). Concerning For FDPD, the finest crust
437 originates from Coyote Lake (8.4 μm), while the coarsest is from Soda Lake (52 μm) (Table S1).
438 Similarly, for aeolian ripples, the mean median particle diameters for both MDPSD and FDPD are finer
439 at Mesquite Lake (167 and 67 μm , respectively) and coarser at Cronese lakes (264 and 234 μm ,
440 respectively) (Table S1). The high degree of particle aggregation observed in crusts, contrasting with

441 the lower aggregation state in ripples, aligns with findings reported for dust-emitting sediments from
442 Morocco by González-Romero et al. (2023).

443 The mean median particle diameters of ~~sediments-crusts~~ from dust-emitting regions collected in the
444 Mojave Desert are similar to those from the Morocco ~~crusts~~ described by González-Romero et al.
445 (2023). Specifically, the mean median MDPD diameter for the Mojave Desert ($92 \pm 74 \mu\text{m}$) closely
446 resembles that of the Morocco Draâ Lower basin ($113 \pm 79 \mu\text{m}$), albeit slightly finer, and is notably
447 coarser than that of Iceland ($55 \pm 62 \mu\text{m}$) (González-Romero et al., 2023, 2024). Furthermore, while
448 the finest crust sampled in the Mojave Desert (Ivanpah with $35 \mu\text{m}$) is almost twice as coarse as slightly
449 coarser than the finest from Morocco (L' Bour with $20 \mu\text{m}$), ~~the differences remain relatively~~
450 ~~small almost 2 times coarser~~. For FDPD, the coarsest crust Icelandic top sediment surface is the
451 coarsest average median particle diameter is from Iceland ($56 \pm 69 \mu\text{m}$), followed by both Morocco
452 and Mojave crusts (37 ± 77 and $37 \pm 48 \mu\text{m}$, respectively). Additionally, average MDPD median
453 diameters of aeolian ripples from ~~the the~~ Mojave Desert sources samples closely resemble those from
454 Morocco (226 and $221 \mu\text{m}$, respectively), while those from Iceland are slightly coarser ($280 \mu\text{m}$).

455 Dry sieved size fractions of dust-emitting sediments show the highest percentage of mass in the 250-
456 500 and 80-250 μm fractions, with minimal mass at 500-1000 μm and 1-2 mm and in the finer fractions
457 (20-40 and $<20 \mu\text{m}$) (Figure 6, Table S2). In both cases, the size fractions from 80 to 500 μm
458 accumulated a total of 75 to 90 % of the total mass fraction (Table S2).

459 Close to the centre of the Soda Lake, where numerous crust samples were collected, before reaching
460 massive crust cementation by evaporite minerals, the FDPD median diameter reaches very fine sizes
461 ($8\text{-}15 \mu\text{m}$) (Figure S1). In contrast, towards the edges of the basin (closer to the mountains surrounding
462 this endorheic lake), the size markedly increases, ranging from 22 to $87 \mu\text{m}$ (Figure S1). Similar
463 patterns, yet with coarser sizes, are observed for the MDPD. As described in previous studies, t
464 the fluctuation of the groundwater table in the centre of the basin leads-can lead to the-a massive
465 precipitation of salts, resulting in the formation of compact crusts (Figure 4) as seen also by other
466 authors (Reynolds et al., 2007; Nield et al., 2016a; Nield et al., 2016b; Urban et al., 2018) that should
467 effectively reduce dust emission. However, at the edges-of this central part, where the precipitation
468 of salts is less frequent, and reworking of the crusts by fluctuations in the groundwater occurs, salty
469 and spongy crusts are formed (Figure 4) (Nield et al., 2016a and Nield et al., 2016b). These spongy
470 crusts, being less compact, are more easily broken by saltating particles, potentially leading to
471 frequent high-salt dust emissions.

472 This-The slight particle size segregation, with finer particles accumulating towards the center of the
473 lake, can be attributed to the transport of sediments from the surrounding mountains to the lake's
474 center by runoff waters during rain episodes. Initially, the coarser particles are deposited, followed by
475 the finer particles that remain suspended in the water for a longer duration particle size segregation,
476 with finer particle diameters towards the centre of the lake, is derived from the transport of sediments
477 from the surrounding mountains to the central part of the lake by runoff waters during rain episodes
478 settling. Nevertheless, the crusts in the surroundings alluvial fans of the Soda Lake ($22\text{-}87 \mu\text{m}$ in the
479 edges compared to $8\text{-}15 \mu\text{m}$ in the centre, Figure S1) are fine enough and surrounded by dunes
480 (availability of saltators for saltation bombardment) to have a high potential dust emission under
481 favourable conditions (Reynolds et al., 2006; Reheis et al., 2009; Urban et al., 2018).

482 3.2. Mineralogy

483 ~~The evaluation of the mineralogy of crusts and aeolian ripples is key identifying potential dust source~~
484 ~~markers in the emitted dust, and investigating size fractionation processes upon transport into the~~
485 ~~basins that may alter mineral contents compared to the background sediment mineralogy.~~

486 Dust-emitting sediments from the Mojave Desert primarily consist of feldspars (41 ± 12 %, including
487 albite/anorthite and microcline), quartz (22 ± 11 %) and clay minerals (18 ± 12 %, such as kaolinite,
488 montmorillonite and illite). Additionally, minor contents of carbonate minerals (6.6 ± 6.6 %),
489 amphibole (pargasite) 4.1 ± 1.5 %, and iron oxides (maghemite/magnetite) (0.77 ± 0.54 %) are
490 observed (Figure 67, Tables 2 and S32). ~~Moreover, at~~ Soda, Mesquite and Cronese lakes, Na-salts
491 such as halite, thenardite, trona, and burkeite are also present, with an average salt content of $5.0 \pm$
492 11 %. Additionally, zeolites ($0.77 \pm 1.1\%$ to 8.5%) including laumontite and analcime are detected at
493 Soda, Cronese, and Coyote lakes (the southern ~~onessites~~), with the highest content observed at
494 Coyote Lake. ~~High amounts of~~ Gypsum ~~are~~ found at Mesquite Lake (15 ± 29 %) (Figure 67, Tables 2
495 and S32). Moreover, Mesquite Lake crusts exhibit high contents of dolomite and calcite ($15 \pm 11\%$)
496 compared to other basins ($3.6 \pm 2.6\%$ to 7.2%) (Table 2).

497 The overall mineral composition of the dust-emitting sediments originates primarily from the source
498 rocks prevalent in the region. These include dominant ~~granitic rocks~~ of Mesozoic ~~granitic rocks~~,
499 as well as pre-Tertiary, Tertiary and Quaternary volcanic ~~rockss~~, and Pre-Cambrian and Mesozoic
500 metamorphic rocks (Figure 1). In the northern, northeastern, and eastern areas of ~~the~~ Mesquite Lake,
501 an important limestone and dolostone massif from the Palaeozoic ~~serves as a significant source of~~
502 ~~sediments (Figure 1)era~~, contributes notably to the high content of calcite and dolomite in the
503 sediments of this lake (Figure 1). ~~The presence of~~ Zeolites ~~content in the sedimentss~~ may be
504 attributed to the weathering of volcanic outcrops in the region or to precipitation in alkaline lakes.
505 ~~This diverse bedrockks mineralogy results in a wide variety of minerals in the dust-emitting sediments.~~
506 ~~The detected form of iron oxide detected in the samples, identified via XRD, is as maghemite.~~
507 ~~However, distinguishing between maghemite and magnetite using XRD is challenging (Vandenberghe~~
508 ~~et al., 2000), and magnetite has been found to be ubiquitous in Mojave dust (Reheis et al., 2009;~~
509 ~~Reynolds et al., 2006).and Therefore, we will refer hereafter to maghemite/magnetite to account for~~
510 ~~the potentialthe presence of both minerals in the samples.~~

511 In comparison to aeolian ripples, the average composition of ~~the selected Mojave Desert~~ crusts shows
512 ~~slightly~~ enrichment in clay minerals (24 ± 11 versus 7.8 ± 2.3 % in crust and ripples, respectively),
513 carbonates (6.6 ± 6.6 versus 1.1 ± 2.2 %), Na-salts (7.3 ± 13 versus 1.1 ± 3.7 %), zeolites (1.2 ± 1.9
514 versus 0.12 ± 0.52 %) and maghemite/magnetite (0.92 ± 0.59 versus 0.49 ± 0.28 %), while being
515 depleted in quartz (16 ± 7.2 versus 32 ± 9.5 %), feldspars (37 ± 9.7 versus 48 ± 13 %) and gypsum (3.1
516 ± 14 versus 4.7 ± 20 %), with similar amphibole content (4.1 ± 1.5 versus 4.1 ± 1.6 %) (Figure 67, Tables
517 2 and S32). ~~Theseis mineralogy enrichment and depletion trends in crusts are observed in all the playa~~
518 ~~lakes, except for Mesquite Lake, which is discussed below.~~

519 ~~The results demonstrate show that crusts, in all cases, have a significant enrichment in clay minerals,~~
520 ~~Na-salts, zeolites, and maghemite, while being depleted in quartz and feldspars compared to ripples,~~
521 ~~except for the anthropogenically disturbed sediments in Mesquite Lake as discussed below (Table 2).~~

522 In ~~the largest dust hotspot~~, Soda Lake, the concentration of Na-salts in crusts increases towards the
523 inner part of the lake, ranging from 5-10 % at the ~~edges margins~~ to 45-50 % in the centre, where
524 compact and fully salt-cemented crusts form. This phenomenon is illustrated in Figure 78, which
525 presents a geological and mineralogical cross-section of Soda Lake. In addition to the water transport
526 to this central part of the basin during the rain episodes, groundwater discharge from the Zzyzx
527 mountains occurs. There, the groundwater table is close to the surface, ~~and the high salinity of the~~
528 ~~aquifer and its interaction with the surface~~ causes the massive ~~precipitation mobilisation~~ of ~~N-Na~~-salts
529 that consolidate the crusts (Figure 4) (Nield et al., 2016b). Cycles of precipitation and dissolution of
530 the salts yield salty spongy crusts (Figure 4) at the edges of these massive crusts, with higher dust
531 emission potential in the degraded salty crusts (Nield et al., 2016a). The very high content of Na-salts
532 content in Soda Lake is attributed to the continuous high Na-S-Cl groundwater ~~supply interaction~~ in
533 the vicinity of Zzyzx, defining Soda Lake as a wet playa lake according to Reynolds et al. (2009) and
534 Urban et al. (2018). On the other hand, Cronese, Coyote, and Ivanpah are categorized as dry lakes.

535 Mesquite Lake features extensive gypsum deposits at the surface, which are a major component of
536 both dunes and crusts. A small gypsum mine operates in Mesquite Lake. The gypsum content in crusts
537 is notably higher at the center (80%) compared to the margins (3-11%). In contrast, the contents of
538 Na-salts and carbonates are greater at the margins (30% and 12-18%, respectively) than at the center
539 (7.5-14% and <0.1-6.9%, respectively). Aeolian ripples at the center of Mesquite Lake exhibit a very
540 high gypsum content, whereas at the margins, these ripples contain higher amounts of quartz,
541 feldspars, and clays than at the center. Despite the presence of the disturbed mine area, most large
542 dust events at Mesquite Lake have been observed to originate from natural (undisturbed) playa
543 surfaces near the margins (Reynolds R., personal communication).

544 Amphiboles in the Mojave Desert, sourced from metamorphic rocks of the area, are homogeneous
545 and can serve as a marker for emitted desert dust in the region. Comparing mineralogy from Mojave
546 Desert crusts to Moroccan surface samples (González-Romero et al., 2023), the former are largely
547 enriched in feldspars, clay minerals, Na-salts, and gypsum, and depleted in quartz and carbonates,
548 with trace proportions of amphibole, zeolites, and maghemite/magnetite. Ripples in the Mojave
549 Desert are depleted in quartz and carbonates, enriched in feldspars, clay minerals, Na-salts, and
550 gypsum, with traces of amphibole, maghemite/magnetite, and zeolites compared to Moroccan
551 ripples. The mineralogy of the Mojave Desert is markedly different from that of Iceland, due to
552 differences in bedrock geology, although both contain feldspars, zeolites, and maghemite/magnetite
553 (González-Romero et al., 2024).

554 Particle aggregation of the dust-emitting sediments from the Mojave Desert samples is, similar to
555 those described by González-Romero et al. (2023) for ~~the Moroccan onessamples~~, is probably likely
556 due to the presence of clays, Na-salts and precipitated carbonates ~~presence~~. This aggregation inhibits
557 aerodynamic entrainment and dust emission should be ~~mostly primarily~~ controlled by saltation
558 bombardment (Shao et al., 1993). According to the XRD analysis, the occurrence of crystalline Fe
559 oxides is limited to maghemite/magnetite in contrast to the hematite/goethite content found in
560 Moroccan crusts (González-Romero et al., 2023). However, due to the XRD low precision on the
561 detection of low contents of minerals such as hematite and goethite, their presence in the samples
562 cannot be ruled out. In fact, both the EMIT standard products (Figure 3), and the Fe mode of
563 occurrence analysis discussed in the next section suggest the presence of hematite and goethite. The
564 occurrence of crystalline Fe oxides is limited to maghemite mainly a weathering product from

565 magnetite, with nohematite, goethite or other Fe oxides (that were not detected by XRD), in contrast
566 to Moroccan crusts (González-Romero et al., 2023).

567 The EMIT standard products (Figure 3) indicate the presence of phyllosilicates such as kaolinite,
568 smectite, montmorillonite, and illite, broadly consistent with our results. Specifically, around Mesquite
569 Lake, where elevated levels of gypsum and carbonates were detected, the EMIT results corroborate
570 the significance of these minerals in the same vicinity. Similarly, in Coyote, Ivanpah, and Cronese Lakes,
571 there is agreement regarding the prevalence of illite and muscovite as the major clay minerals,
572 alongside kaolinite. However, discrepancies arise in Soda Lake, where EMIT identifies a dominant
573 presence of montmorillonite, contrasting with our XRD results indicating a predominance of illite,
574 muscovite, and kaolinite. While Tetracorder identified predominant montmorillonite, illite, muscovite
575 and kaolinite could be on the order of 30% of the montmorillonite abundance and not show in the
576 EMIT spectra without a more sophisticated non-linear radiative transfer model to find the relative
577 abundances of these two minerals. This is due to the relative absorption strengths of the spectral
578 features of these minerals relative to those in montmorillonite. While our XRD analyses highlight the
579 presence of maghemite/magnetite, these minerals do not present clear absorbing features in the
580 spectral range of the EMIT instrument and are not considered within the 10 EMIT standard minerals.
581 In contrast to the XRD results, EMIT highlights the significant presence of goethite in the northern
582 sources (Mesquite and Ivanpah Lakes). Conversely, in the southern sources (Soda, Cronese, and
583 Coyote Lakes), EMIT highlights a major mixture of Fe²⁺ and Fe³⁺ species. The limited precision of XRD
584 for low proportions of Fe oxides, underscores the need for complementary techniques and analyses
585 to bolster our findings.

586 The mineralogical composition of the dry size-segregated fractions of the dust-emitting sediments is
587 outlined in Table S4. The findings indicate that there is no significant size enrichment process in crusts;
588 rather, there exists a relatively uniform distribution of quartz, feldspars, zeolites, and Fe oxides across
589 all size fractions (Figure 6). A slight, albeit not significant, enrichment of carbonates and clays is
590 observed, along with a slight depletion of Na-salts and gypsum in the finer fractions (<20 µm).
591 Additionally, pargasite shows a slight enrichment in the 40-80 µm fraction. In contrast, for aeolian
592 ripples, quartz exhibits significant enrichment in the coarser fraction (250-500 µm) and depletion in
593 the finer ones (<80 µm). Regarding carbonates, clays, and Fe oxides, there is an enrichment towards
594 the finer fractions (<20 µm), while the content of feldspars remains relatively homogeneous. Pargasite
595 content increases in the 40-80 µm fraction, and Na-salts and gypsum are either not detected or
596 present in trace amounts (Figure 6). The notable disparity in the enrichment factor between crusts
597 and aeolian ripples is partly attributed to the reduced amount of sand and the differing cohesion
598 states: crusts exhibit high cohesion, resulting in a homogenized mineralogy across size fractions (as
599 aggregates form a homogeneous concretion of minerals), while aeolian ripples display lower or
600 negligible aggregation, leading to a slightly more heterogeneous mineralogy across size fractions
601 compared to crusts.

602 3.3. Mode of occurrence of Fe

603 The average content of Fe_T in the Mojave crusts is 3.0 ± 1.3 wt %, while for aeolian ripples is 1.9 ± 1.1
604 wt %. Among these crusts, 1.8 ± 0.92 % of the Fe_T occurs as FeA, 17 ± 7.2 % as FeD, 2.1 ± 1.2 as FeM
605 and 79 ± 8.5 % as FeS (Tables 3 and S53). Aeolian ripples have very similar contents and modes of
606 occurrence of Fe across in the analysed samples of the Mojave Desert.

607 Among the crusts, Ivanpah has the highest FeT content at 4.9 %, followed by Cronese and Coyote lakes
608 (3.7 ± 1.2 % and 3.5 %, respectively), with Soda Lake showing a similar content (3.1 ± 1.2 %). Mesquite
609 has the lowest FeT (1.6 ± 0.53 %), probably due to dilution of detrital Fe-bearing minerals with salts
610 and gypsum. FeS is the dominant mode of occurrence in most lakes, ranging from 68 % (1 sample) at
611 Ivanpah, to 74 ± 3.5 and 74 ± 13 % at Mesquite and Cronese, and to 83 ± 2.8 and 82 % at Soda and
612 Coyote lakes. The FeD is higher at Ivanpah (29 %), Cronese Lakes (21 ± 11 %) and Mesquite Lake (21 ±
613 11 (and 20 ± 2.7 %), and lower than at Soda and Coyote lakes (14 ± 2.5 and 14 %). ~~The content of~~ FeM
614 is higher at Mesquite Lake (3.7 ± 1.2 %), followed by Cronese and Coyote lakes (2.3 ± 1.1 and 2.4 %),
615 and Soda (1.5 ± 0.49 %) and Ivanpah Lakes (0.82 %). Finally, FeA is higher at Cronese Lake (2.4 ± 0.99
616 %), compared to Coyote, Mesquite, Soda and Ivanpah lakes (1.8, 1.8 ± 0.93, 1.5 ± 0.81 and 1.4 %)
617 (Tables 3 and S53). Crusts are enriched in FeT, FeD and FeA compared to ripples, while ripples are
618 enriched in FeM and FeS (Tables 3 and S53).

619 Thus Overall, the bulk Fe content in crusts is driven by structural Fe from clays and amphiboles (as
620 deduced from the high correlation shown in Figure 8a9a), followed by small proportions of hematite
621 and goethite (not detected by XRD), which are clearly higher at the northern lakes Ivanpah and
622 Mesquite lakes (consistent with the highlighted presence of goethite in the EMIT standard products),
623 probably due to the Precambrian and Cambrian metamorphic rocks that supply sediments.
624 Furthermore, the easily exchangeable Fe is also driven by clay minerals (Figure 8b9b).

625 Compared to crusts in other arid regions analysed by González-Romero et al. (2023, 2024), the
626 analysed Mojave Desert crusts have similar FeT content ~~to~~ than Moroccan crusts but are much lower
627 than the Iceland top sediments (loose surface sediments in Iceland according to González-Romero et
628 al. (2024)) (3.0 ± 1.3, 3.6 ± 0.71 and 9.5 ± 0.39 %, for Mojave, Morocco, and Iceland respectively). The
629 proportion of FeS in FeT is similar to the Icelandic sediments but higher than in Moroccan samples (79
630 ± 8.5 and 79 ± 6.5 %, and 67 ± 2.4, respectively). The proportion of FeM is clearly lower than that of
631 Iceland, but higher than that of Morocco (2.1 ± 1.2 and 16 ± 5.4 %, for Mojave and Iceland; Morocco
632 proportion is negligible). The FeD proportion is intermediate between Morocco and Iceland (17 ± 7.2,
633 31 ± 2.3, 3.5 ± 1.5 %, respectively), while the FeA proportion is similar to both Morocco and Iceland
634 crusts (1.8 ± 0.92, 1.3 ± 0.39 and 1.9 ± 0.55 %, respectively) (Figure 910).

635 **4. Discussion and cConclusions**

636 The playa lakes sampled within the Mojave Desert can serve as significant dust-emitting sources in the
637 region. Descriptions provided by Urban et al. (2018) and satellite imagery (Figure 2) confirm the
638 presence of desert dust emissions originated from these areas. The lithology, geological/tectonic
639 evolution, and past and current climate conditions collectively contribute to the formation of these
640 dust sources in the Mojave Desert.

641 Dust-emitting sediments in this region predominantly stem from substratum rocks, comprising mainly
642 granitic and volcanic formations, along with metamorphic Pre-Cambrian, Cambrian, Paleozoic, and
643 Mesozoic rocks. Endorheic basins, shaped by faulting during the Tertiary-Quaternary period,
644 accumulated fine sediments through erosion, transportation, and deposition processes. Wetter
645 conditions prevailing during the Pleistocene epoch led to the formation of deep lakes within the
646 basins, which gradually desiccated as the climate evolved. These arid conditions rendered the playa
647 lakes susceptible to dust emission under specific atmospheric conditions. Notably, a particle size

648 segregation is observed, transitioning from coarser sediments in the proximal alluvial areas towards
649 finer particle crusts within the central regions of the lakes. In the playa lakes, finer sediments
650 accumulate towards the centre of the lakes due to flood events inundating the central areas and
651 ponding, which facilitates the deposition of coarser particles followed by top finer sediment sizes.

652 According to the conceptual model depicted in Figure 1011, the finer dust particle size distributions
653 (FDPSD) range from 8.4 to 99 μm inside Soda Lake and 46 to 111 μm outside Soda Lake, (MDPSD),
654 underscoring this sedimentation process. Comparisons with conceptual models proposed for other
655 regions, such as those by González-Romero et al. (2023, 2024) for locations in Morocco and Iceland,
656 reveal a similar transport fractionation phenomenon occurring in the Mojave Desert. These crusts,
657 observed within Soda Lake, show enrichment in clay minerals, carbonate minerals, salts, and iron
658 oxides, while experiencing depletion in coarser constituents such as feldspars and quartz.

659 In the Mojave Desert, there are two distinct types of playa lakes, characterized as wet and dry, ~~are~~
660 ~~delineated based~~ depending on the regime of the groundwater table and its ~~interaction~~ relationship
661 with the surface, ~~as discussed as described~~ by Reynolds et al. (2007 and 2009), Buck et al. (2011), Nield
662 et al. (2016a and b), Urban et al. (2018) and Goudie (2018). Understanding the groundwater table
663 regime is fundamental in this region due to its profound ~~influence~~ relation on the porosity of the crust
664 and its consequential impact on mineralogy, including the precipitation and enrichment of salts (Figure
665 1011). This dynamic contrasts sharply with other conceptual models, where the relationship between
666 crust formation and the groundwater table is either minimal or absent entirely. For instance, there is
667 no or little relation between crusts and groundwater table in Morocco, and in Iceland, where the water
668 regime is largely influenced by floodings from glaciers (González-Romero et al., 2023, 2024). In wet
669 playa lakes like Soda Lake, the presence of salty crusts, whether massive or spongy, is significantly
670 pronounced. Conversely, in dry playa lakes such as Ivanpah, Coyote, and Cronese, the ~~influence~~
671 relationship of salt crusts is notably less prominent as the proportion of Na-salts is lower (see Figure
672 1011). ~~Mesquite Lake serves as a poignant example of an anthropogenically disturbed playa lake,~~
673 ~~highlighting the importance of monitoring dust changes resulting from human actions in such~~
674 ~~environments.~~

675 At Soda Lake, ~~a wet playa,~~ a hard crust, measuring up to 0.5 meters in thickness (Figure 3), forms
676 through the extensive precipitation of Na-salts, particularly near the Zzyzx area, where a relatively
677 constant ~~supply~~ mobilisation of salts is ~~provided due to~~ by the water table evaporation or vapour
678 discharge from deeper parts of the sediment towards the surface (Nield et al., 2015, 2016a and b).
679 Along the edges of this massive crusty area, the frequent oscillation of the water table may results in
680 the precipitation and dissolution of salts in lower quantities compared to the center, leading to the
681 formation of weaker crusts characterized by high porosity. These porous crusts ~~may~~ can contribute to
682 an increased dust emission rate compared to the hard salt crusts found in the center. Dry lakes such
683 as Ivanpah, Cronese, and Coyote do not exhibit the formation of spongy crusts due to the low
684 concentrations of salts. In wet playas, strong dust emission may happen when very strong winds rip
685 off thin crusts exposing the fine-grained sediment beneath including lithogenic and salt mineral
686 particles (Rich Reynolds, personal communication).

687 Particle aggregation facilitated by diagenetic salts and carbonate minerals is prevalent in the samples
688 dust-emitting sediments of the Mojave Desert, akin to the equivalent sediments found in the
689 Moroccan Sahara. The average grain size of the crusts from both regions is similar, with MDPSD values

690 of $113 \pm 79 \mu\text{m}$ for Morocco and $92 \pm 74 \mu\text{m}$ for the Mojave Desert, and FDPSP values of $37 \pm 77 \mu\text{m}$
691 and $37 \pm 48 \mu\text{m}$, respectively. These patterns contrast with the lower aggregation state and finer
692 MDPSD observed in Icelandic dust ($55 \pm 62 \mu\text{m}$) (Table 4).

693 In terms of mineralogy, crusts from the Mojave Desert are enriched in feldspars, clay minerals, Na-
694 salts, and gypsum, whereas crusts from the Moroccan Sahara are enriched in quartz and carbonates
695 (Table 4). The mineralogy of Icelandic top sediments ([loose surface sediments in Iceland according to](#)
696 [González-Romero et al. \(2024\)](#)) differs due to their volcanic origin; however, both the Mojave Desert
697 [crusts](#) and Icelandic top sediments contain similar amounts of zeolites. Salt enrichment in the crusts
698 is primarily attributed to interactions with the groundwater table [as suggested by literature shown in](#)
699 [previous studies \(Niell et al. \(2016a and b\), Urban et al. \(2018\) and Goudie \(2018\)\)](#)(Figure 1011).

700 The total iron content (FeT) remains consistent throughout the [samples collected in the](#) Mojave
701 Desert, with slightly higher levels observed in the Ivanpah crust, albeit diluted by the high salt content
702 in the wet playa lake crusts or the elevated gypsum content in the [anthropogenically disturbed](#)
703 Mesquite Lake. While the total Fe content is comparable between the Mojave Desert and Moroccan
704 Sahara crusts (3.0 and 3.6 wt %, respectively), it is substantially lower than in Icelandic top sediments
705 (9.3 wt %). Exchangeable Fe proportions in FeT are similar among the three environments. The
706 proportion of Fe from hematite and goethite in Mojave Desert crusts fall between those of Moroccan
707 Sahara crusts and Icelandic top sediments (17, 31, and 0.5 wt %, respectively). The proportion of
708 [maghemite/magnetite](#) in Mojave Desert crusts is much lower compared to Icelandic top sediments
709 (2.1 and 15 %, respectively). Finally, the proportion of structural Fe in the samples is similar across the
710 three environments.

711 In conclusion, ~~the the~~ dust-emitting sediments [collected](#) from the Mojave Desert exhibit distinct
712 signatures in mineralogy and [modes of Fe mode of occurrence occurrences of Fe](#) compared to those
713 from the Moroccan Sahara, despite similar particle sizes. These differences can influence emitted dust
714 properties, and associated impacts. Similarities in fully disturbed and minimally disturbed particle size
715 distributions support comparable dust emission mechanisms, with saltation bombardment playing a
716 prominent role. ~~The mineralogy and Fe mode of occurrence of Mojave Desert dust significantly differ~~
717 ~~from Icelandic dust, potentially resulting in different radiative effects and oceanic and terrestrial~~
718 ~~fertilization.~~

719 **Code availability.** The Tetracorder code used in this paper is provided by Clark (2023,
720 <https://github.com/PSI-edu/spectroscopy-tetracorder>).

721 **Data availability.** Data used in this paper are given in the main paper itself and in the Supplement. If
722 needed, data are also available upon request by emailing the authors.

723 **Author contribution.** Sample permits were obtained by BLE, RG and AK. The samples were collected
724 by CPG-P, AGR, AK, RG and XQ and analysed by AGR, MHC and NM. EMIT mineralogy maps were
725 produced by RG, PB and RC. PG provided the FoO map. AGR analyzed the data and wrote of the original
726 draft manuscript supervised by CPG-P and XQ. CPG-P and XQ re-edited the manuscript and all authors
727 contributed to data discussion, reviewing and manuscript finalization.

728 **Competing interests.** At least one of the (co-)authors is a member of the editorial board of
729 Atmospheric chemistry and Physics.

730 Acknowledgements

731 [We thank Richard Reynolds and another anonymous reviewer for the helpful comments and](#)
732 [suggestions to improve the manuscript.](#)

733 The field campaign and its associated research, including this work, was funded by the European
734 Research Council under the Horizon 2020 research and innovation programme through the ERC
735 Consolidator Grant FRAGMENT (grant agreement No. 773051) and the AXA Research Fund through
736 the AXA Chair on Sand and Dust Storms at BSC. CGF was supported by a PhD fellowship from the
737 Agència de Gestió d'Ajuts Universitaris i de Recerca (AGAUR) grant 2020_FI B 00678. KK was funded
738 by the Deutsche Forschungsgemeinschaft (DFG, German Research Foundation) – 264907654;
739 416816480. MK has received funding through the Helmholtz Association's Initiative and Networking
740 Fund (grant agreement no. VH-NG-1533). We acknowledge the EMIT project, which is supported by
741 the NASA Earth Venture Instrument program, under the Earth Science Division of the Science Mission
742 Directorate. We are grateful to Claire Blaske and Sahil Azad for assistance sampling in the Mojave
743 National Preserve. Samples within the preserve were collected under permit MOJA-2022-SCI-0034.
744 We thank Rose Pettiette at the BLM office in Needles, CA, for advice and allowing sampling on BLM
745 land. We thank Jason Wallace and Anne Kelly from CSU Desert Studies Center at Zzyzx for their support
746 during the campaign. BLE, RG, and AMK thank the Resnick Sustainability Institute at Caltech for partial
747 support. Without all of them, the sampling campaign would not have been successfully feasible.

748 5. References

- 749 [Alfaro, S. C., Gaudichet, A., Gomes, L., & Maillé, M. \(1997\). Modeling the size distribution of a soil](#)
750 [aerosol produced by sandblasting. *Journal of Geophysical Research: Atmospheres*, 102\(D10\),](#)
751 [11239-11249.](#)
- 752 Arnalds, Ó., Olafsson, H. and Dagsson-Waldhauserova, P.: Quantification of iron-rich volcanogenic
753 dust emissions and deposition over the ocean from Icelandic dust sources, *Biogeosciences*,
754 11, 6623-6632. <https://doi.org/10.5194/bg-11-6623-2014>, 2014.
- 755 Atkinson, J. D., Murray, B. J., Woodhouse, M. T., Whale, T. F., Baustian, K. J., Carslaw, K. S., ... & Malkin,
756 T. L.: The importance of feldspar for ice nucleation by mineral dust in mixed-phase clouds.
757 *Nature*, 498(7454), 355-358, 2013.
- 758 [Baddock, M. C., Ginoux, P., Bullard, J. E., & Gill, T. E. \(2016\). Do MODIS-defined dust sources have a](#)
759 [geomorphological signature?. *Geophysical Research Letters*, 43\(6\), 2606-2613.](#)
- 760 Baldo, C., Formenti, P., Nowak, S., Chevaillier, S., Cazaunau, M., Pangui, E., Di Baggio, C., Doussin, J.F.,
761 Ignatyev, K., Dagsson-Waldhauserova, P., Arnalds, O., MacKenzie, A.R., Shi, Z.: Distinct
762 chemical and mineralogical composition of Icelandic dust compared to Northern African and
763 Asian dust. *Atmospheric Chemistry and Physics*, 20, 13521-13539, 2020.
- 764 Bauer, S. E., & Koch, D.: Impact of heterogeneous sulfate formation at mineral dust surfaces on aerosol
765 loads and radiative forcing in the Goddard Institute for Space Studies general circulation
766 model. *Journal of Geophysical Research: Atmospheres*, 110(D17), 2005.
- 767 Beadoing, H., Rodell, M., & NASA/GSFC/HSL: GLDAS Noah Land Surface Model L4 monthly 0.25 x 0.25
768 degree, Version 2.1 [dataset]. NASA Goddard Earth Sciences Data and Information Services
769 Center. 2020. <https://doi.org/10.5067/SXAVCZFAQLNO>.

770 [Buck, B.J., King, J. and Etyemezian, V., 2011. Effects of salt mineralogy on dust emissions, Salton Sea,](#)
771 [California. Soil Science Society of America Journal, 75\(5\), pp.1971-1985.](#)

772 [Bullard, J. E., Harrison, S. P., Baddock, M. C., Drake, N., Gill, T. E., McTainsh, G., & Sun, Y. \(2011\).](#)
773 [Preferential dust sources: A geomorphological classification designed for use in global dust-](#)
774 [cycle models. Journal of Geophysical Research: Earth Surface, 116\(F4\).](#)

775 Chatziparaschos, M., Daskalakis, N., Myriokefalitakis, S., Kalivitis, N., Nenes, A., Gonçalves Ageitos, M.,
776 Costa-Surós, M., Pérez García-Pando, C., Zanolli, M., Vrekoussis, M. & Kanakidou, M.: Role of K-
777 feldspar and quartz in global ice nucleation by mineral dust in mixed-phase clouds.
778 Atmospheric Chemistry and Physics, 23(3), 1785-1801, 2023.

779 Cheary, R.W., Coelho, A.: A fundamental parameters approach to X-ray line profile fitting. Journal of
780 Applied Crystallography 25, 109–121, 1992.

781 [Claquin, T., Schulz, M., & Balkanski, Y. J. \(1999\). Modeling the mineralogy of atmospheric dust sources.](#)
782 [Journal of Geophysical Research: Atmospheres, 104\(D18\), 22243-22256.](#)

783 [Clark, Roger N., 2024, PSI-edu/spectroscopy-tetracorder: Tetracorder 5.27 with expert systems to](#)
784 [5.27e + specpr, spectral libraries, and radiative transfer models \(v5.27.0\). Zenodo.](#)
785 <https://doi.org/10.5281/zenodo.11204505>

786 [Clark, R. N., G. A. Swayze, K. E. Livo, P. Brodrick, E. Noe Dobrea, S. Vijayarangan, R. O. Green, D.](#)
787 [Wettergreen, A. Candela, A. Hendrix, C. P. Garcia-Pando, N. Pearson, M. D. Lane, A. Gonzalez-](#)
788 [Romero, X. Querol, and the EMIT and TREX teams, 2024. Imaging spectroscopy: Earth and](#)
789 [planetary remote sensing with the PSI Tetracorder and expert systems: from Rovers to EMIT](#)
790 [and Beyond Planetary Science Journal in review.](#)

791 Crumeyrolle, S., Gomes, L., Tulet, P., Matsuki, A., Schwarzenboeck, A., and Crahan, K.: Increase of the
792 aerosol hygroscopicity by cloud processing in a mesoscale convective system: a case study
793 from the AMMA campaign, Atmos. Chem. Phys., 8, 6907–6924, [https://doi.org/10.5194/acp-](https://doi.org/10.5194/acp-8-6907-2008)
794 [8-6907-2008](https://doi.org/10.5194/acp-8-6907-2008), 2008.

795 De la Torre, A.G., Bruque, S., Aranda, M.A.G.: Rietveld quantitative amorphous content analysis.
796 Journal of Applied Crystallography, 34:196-202, 2001.

797 De Longueville, F., Hountondji Y.C., Henry S., Ozer P.: What do we know about effects of desert dust
798 on air quality and human health in West Africa compared to other regions?. Sci. Total Environ.,
799 409, 1–8, 2010.

800 Dibblee T.W.: Areal geology of the western mojave desert California. Geological Survey Professional
801 paper, 522, <https://doi.org/10.3133/pp522>, 1967.

802 Di Biagio, C., Formenti, P., Balkanski, Y., Caponi, L., Cazaunau, M., Pangui, E., Journet, E., Nowak, S.,
803 Andreae, M.O., Kandler, K., Saeed, T., Piketh, S., Seibert, D., Williams, E., Doussin, J.F.: Complex
804 refractive indices and single-scattering albedo of global dust aerosols in the shortwave
805 spectrum and relationship to size and iron content. Atmos. Chem. Phys., 19, 15503-15531.
806 <https://doi.org/10.5194/acp-19-15503-2019>, 2019.

807 Eghbal, M.K., Southard, R.J.: Mineralogy of Aridisols on Dissected Alluvial Fans, Western Mojave
808 Desert, California. Soil Science Society of America Journal, 57, pp. 538-544, 1993.

809 Engelbrecht, J.P., Moosmüller, H., Pincock, S., Jayanty, R.K.M., Lersch, T., Casuccio, G.: Technical note:
810 Mineralogical, chemical, morphological, and optical interrelationships of mineral dust re-
811 suspensions. Atmos. Chem. Phys., 16, 10809-10830. [https://doi.org/10.5194/acp-16-10809-](https://doi.org/10.5194/acp-16-10809-2016)
812 [2016](https://doi.org/10.5194/acp-16-10809-2016), 2016.

813 [Floyd, K. W., & Gill, T. E. \(2011\). The association of land cover with aeolian sediment production at](#)
814 [Jornada Basin, New Mexico, USA. Aeolian Research, 3\(1\), 55-66.](#)

815 Formenti, P., Caquineau, S., Chevaillier, S., Klaver, A., Desboeufs, K., Rajot, J.L., Belin, S., Briois, V.:
816 Dominance of goethite over hematite in iron oxides of mineral dust from Western Africa:
817 Quantitative partitioning by X-ray absorption spectroscopy. *J. Geophys. Res. Atmos.*, 119,
818 12740-12754, <https://doi.org/10.1002/2014jd021668>, 2014.

819 Frank, T.D., Di Girolamo, L., Geegan, S.: The spatial and temporal variability of aerosol optical depths
820 in the Mojave desert of southern California. *Remote Sensing of Environment*, 107, 1-2, 54-64,
821 <https://doi.org/10.1016/j.rse.2006.06.024>, 2007.

822 [Ginoux, P., Chin, M., Tegen, I., Prospero, J. M., Holben, B., Dubovik, O., & Lin, S. J. \(2001\). Sources and](#)
823 [distributions of dust aerosols simulated with the GOCART model. *Journal of Geophysical*](#)
824 [Research: Atmospheres](#), 106(D17), 20255-20273.

825 Ginoux, P., Prospero, J.M., Gill, T.E., Hsu, N.C., Zhao, M.: Global-scale attribution of anthropogenic and
826 natural dust sources and their emission rates based on MODIS Deep Blue aerosol products.
827 *Rev. Geophys.*, 50, RG3005, doi:10.1029/2012RG000388, 2012.

828 Goldstein, H.L., Breit, G.N., & Reynolds, R.L.: Controls on the chemical composition of saline surface
829 crusts and emitted dust from a wet playa in the Mojave Desert (USA). *Journal of Arid*
830 *Environments*, 140, 50-66, 2017.

831 [González-Flórez, C., Klose, M., Alastuey, A., Dupont, S., Escribano, J., Etyemezian, V., ... & Pérez García-](#)
832 [Pando, C. \(2022\). Insights into the size-resolved dust emission from field measurements in the](#)
833 [Moroccan Sahara. *Atmospheric Chemistry and Physics Discussions*, 2022, 1-65.](#)

834 González-Romero, A., González-Florez, C., Panta, A., Yus-Díez, J., Reche, C., Córdoba, P., Moreno, N.,
835 Alastuey, A., Kandler, K., Klose, M., Baldo, C., Clark, R.N., Shi, Z.B., Querol, X., Pérez García-
836 Pando, C.: Variability in grain size, mineralogy, and mode of occurrence of Fe in surface
837 sediments of preferential dust-source inland drainage basins: The case of the Lower Drâa
838 Valley, S Morocco. *Atmos. Chem. Phys.*, 23, 15815–15834, [https://doi.org/10.5194/acp-23-](https://doi.org/10.5194/acp-23-15815-2023)
839 [15815-2023](https://doi.org/10.5194/acp-23-15815-2023), 2023.

840 González-Romero, A., González-Florez, C., Panta, A., Yus-Díez, J., Córdoba, P., Alastuey, A., Moreno,
841 N., Kandler, K., Klose, M., Clark, R.N., Ehlmann, B.L., Greenberger, R., Keebler, A.M., Brodick,
842 P., Green, R., Querol, X., Pérez García-Pando, C.: Probing Iceland's Dust-Emitting Sediments:
843 Particle Size Distribution, Mineralogy, Cohesion, Fe Mode of Occurrence, and Reflectance
844 Spectra Signatures. *Atmospheric Chemistry and Physics*. EGUSPHERE [Preprint], 2024.

845 Goudie, A.: Dust storms and ephemeral lakes. *Desert*, 23(1), 153-164, 2018.

846 Goudie, A.S. & Middleton, N.J.: Desert dust in the global system. Springer, Heidelberg. ISBN 978-786
847 3-540-32355-6, 288 pp, 2006.

848 Green R.O., Mahowald N., Ung C., Thompson D.R., Bator L., Bennet M., Zan J.: The earth surface
849 mineral dust source investigation: an earth science imaging spectroscopy mission. In: IEEE
850 Aerospace Conference Proceedings. IEEE Computer Society.
851 <https://doi.org/10.1109/AERO47225.2020.9172731>. 2020.

852 Harrison, A. D., Lever, K., Sanchez-Marroquin, A., Holden, M. A., Whale, T. F., Tarn, M. D., ... & Murray,
853 B. J.: The ice-nucleating ability of quartz immersed in water and its atmospheric importance
854 compared to K-feldspar. *Atmospheric Chemistry and Physics*, 19(17), 11343-11361, 2019.

855 [Hettiarachchi, E., Reynolds, R. L., Goldstein, H. L., Moskowitz, B., & Rubasinghege, G. Bioavailable iron](#)
856 [production in airborne mineral dust: Controls by chemical composition and solar flux.](#)
857 [Atmospheric environment](#), 205, 90-102, 2019.

858 [Hettiarachchi, E., Ivanov, S., Kieft, T., Goldstein, H. L., Moskowitz, B. M., Reynolds, R. L., &](#)
859 [Rubasinghege, G. Atmospheric processing of iron-bearing mineral dust aerosol and its effect](#)

860 [on growth of a marine diatom, *Cyclotella meneghiniana*. *Environmental Science & Technology*,](#)
861 [55\(2\), 871-881, 2020.](#)

862 Honke, J.S., Pigati, J.S., Wilson, J., Bright, J., Goldstein, H.L., Skipp, G.L., Reheis, M.C., Havens, J.C.: Late
863 Quaternary paleohydrology of desert wetlands and pluvial lakes in the Soda Lake basin, central
864 Mojave Desert, California (USA). *Quat. Sci. Rev.*, 216, pp. 89-106,
865 10.1016/j.quascirev.2019.05.021, 2019.

866 Ibáñez, J., Font, O., Moreno, N., Elvira, J.J., Alvarez, S., Querol, X.: Quantitative Rietveld analysis of the
867 crystalline and amorphous phases in coal fly ashes. *Fuel*, 105: 314-317, 2013.

868 Jennings, C.W., Burnett, J.L., and Troxel, B.W.: Geologic map of California: Trona sheet. California
869 Division of Mines and Geology, Geologic Atlas of California, GAM-23, 1:250.000, 1962.

870 Jickells, T. D., An, Z. S., Andersen, K. K., Baker, A. R., Bergametti, G., Brooks, N., ... & Torres, R.: Global
871 iron connections between desert dust, ocean biogeochemistry, and climate. *science*,
872 308(5718), 67-71, 2005.

873 [Journet, E., Balkanski, Y., & Harrison, S. P. \(2014\). A new data set of soil mineralogy for dust-cycle](#)
874 [modeling. *Atmospheric Chemistry and Physics*, 14\(8\), 3801-3816.](#)

875 Karanasiou, A., Moreno, N., Moreno, T., Viana, M., de Leeuw, F., Querol, X.: Health effects from Sahara
876 dust episodes in Europe: Literature review and research gaps. *Environ. Int.* 47, 107–14, 2012.

877 Kok, J.F., Adebisi, A.A., Albani, S., Balkanski, Y., Checa-Garcia, R., Chin, M., Colarco, P.R., Hamilton, D.S.,
878 Huang, Y., Ito, A., Klose, M., Li, L., Mahowald, N.M., Miller, R.L., Obiso, V., Pérez García-Pando,
879 C., Rocha-Lima, A., Wan, J.S.: Contribution of the world's main dust source regions to the
880 global cycle of desert dust, *Atmos. Chem. Phys.*, 21, 8169–8193, [https://doi.org/10.5194/acp-](https://doi.org/10.5194/acp-21-8169-2021)
881 [21-8169-2021](https://doi.org/10.5194/acp-21-8169-2021), 2021.

882 Laurent, B., Marticorena, B., Bergametti, G., Léon, J.F., Mahowald, N.M.: Modeling Mineral Dust
883 Emissions from the Sahara Desert Using New Surface Properties and Soil Database *J. Geophys.*
884 *Res.*, 113, D14218, 2008.

885 [Li, L., Mahowald, N. M., Miller, R. L., Pérez García-Pando, C., Klose, M., Hamilton, D. S., ... & Thompson,](#)
886 [D. R. \(2021\). Quantifying the range of the dust direct radiative effect due to source mineralogy](#)
887 [uncertainty. *Atmospheric chemistry and physics*, 21\(5\), 3973-4005.](#)

888 Machiels, L., Mertens, G., Elsen, J.: Rietveld Refinement strategy for Quantitative Phase analysis of
889 Partially Amorphous zeolitized tuffaceous. *GEOLOGICA BELGICA* 13,3, 183-196, 2010.

890 Madsen, I.C., Scarlett, N.V.Y., Cranswick, L.M.D., Lwin, T.: Outcomes of the international union of
891 crystallography commission on powder diffraction round robin on quantitative phase analysis:
892 Samples 1a to 1h. *J. Appl. Crystallogr.*, 34, pp. 409-426, 2001.

893 Mahowald, N.M., Baker, A.R., Bergametti, G., Brooks, N., Duce, R.A., Jickells, T.D., Kubilay, N.,
894 Prospero, J.M., Tegen, I.: Atmospheric global dust cycle and iron inputs to the ocean, *Global*
895 *Biogeochem. Cy.*, 19(4), GB4025, doi:10.1029/2004GB002402, 2005.

896 Matsui, H., Yamane, M., Tonami, T., Nagami, T., Watanabe, K., Kishi, R., Kitagawa, Y., Nakano, M.:
897 Theoretical study on gigantic effect of external static electric field application on nonlinear
898 optical properties of 1,2,3,5-dithiadiazolyl π -radical dimer. *Mater. Chem. Front.*, 2, 785– 790,
899 DOI: 10.1039/C7QM00549K, 2018.

900 Miller, D.M., Menges, C.M., and Lidke, D.J.: Generalized surficial geologic map of the Fort Irwin area,
901 San Bernardino County, California, U.S. Geological Survey, Open-File Report OF-2013-1024-B,
902 1:100.000, 2014.

903 Miller, D.M., Dudash, S.L., & McGeehin, J.P.: Paleoclimate record for Lake Coyote, California, and the
904 Last Glacial Maximum and deglacial paleohydrology (25 to 14 cal ka) of the Mojave River. *S.W.*

905 Starratt, M.R. Rosen (Eds.), From Saline to Freshwater: The Diversity of Western Lakes in Space
906 and Time: Geologic Society of America Special Paper 536, pp. 1-20, 2018.

907 [Nield, J.M., Bryant, R.G., Wiggs, G.F., King, J., Thomas, D.S., Eckardt, F.D., and Washington, R. The
908 dynamism of salt crust patterns on playas. *Geology*, 43\(1\), pp.31-34, 2015.](#)

909 [Nield, J.M., Neuman, C.M., O'Brien, P., Bryant, R.G., and Wiggs, G.F. Evaporative sodium salt crust
910 development and its wind tunnel derived transport dynamics under variable climatic
911 conditions. *Aeolian Research*, 23, pp.51-62, 2016.](#)

912 [Nield, J.M., Wiggs, G.F., King, J., Bryant, R.G., Eckardt, F.D., Thomas, D.S. and Washington, R. Climate–
913 surface–pore-water interactions on a salt crusted playa: implications for crust pattern and
914 surface roughness development measured using terrestrial laser scanning. *Earth Surface
915 Processes and Landforms*, 41\(6\), pp.738-753, 2016.](#)

916 [Obiso, V., Gonçalves Ageitos, M., Pérez García-Pando, C., Perlwitz, J. P., Schuster, G. L., Bauer, S. E., ...
917 & Miller, R. L. \(2024\). Observationally constrained regional variations of shortwave absorption
918 by iron oxides emphasize the cooling effect of dust. *Atmospheric Chemistry and Physics*, 24\(9\),
919 5337-5367.](#)

920 [Panta, A., Kandler, K., Alastuey, A., González-Flórez, C., González-Romero, A., Klose, M., ... & Pérez
921 García-Pando, C. \(2022\). Insights into the single particle composition, size, mixing state and
922 aspect ratio of freshly emitted mineral dust from field measurements in the Moroccan Sahara
923 using electron microscopy. *Atmospheric Chemistry and Physics Discussions*, 2022, 1-40.](#)

924 [Paulot, F., Ginoux, P., Cooke, W. F., Donner, L. J., Fan, S., Lin, M. Y., ... & Horowitz, L. W. \(2016\).
925 Sensitivity of nitrate aerosols to ammonia emissions and to nitrate chemistry: implications for
926 present and future nitrate optical depth. *Atmospheric Chemistry and Physics*, 16\(3\), 1459-
927 1477.](#)

928 Pérez, C., Nickovic, S., Pejanovic, G., Baldasano, J. M., & Özsoy, E.: Interactive dust-radiation modeling:
929 A step to improve weather forecasts. *Journal of Geophysical Research: Atmospheres*,
930 111(D16), 2006.

931 Pérez García-Pando, C., Stanton, M.C., Diggle, P.J., Trzaska, S., Miller, R.L., Perlwitz, J.P., Baldasano,
932 J.M., Cuevas, E., Ceccato, P., Yaka, P., Thomson, M.C.: Soil dust aerosols and wind as predictors
933 of seasonal meningitis incidence in Niger. *Environ. Health Perspect.* 122, 7679-686, 2014.

934 Perlwitz, J.P., Pérez García-Pando, C., and Miller, R.L.: Predicting the mineral composition of dust
935 aerosols – Part 1: Representing key processes. *Atmos. Chem. Phys.*, 15, 11593–11627,
936 <https://doi.org/10.5194/acp-15-11593-2015>, 2015.

937 Potter, C. and Coppernoll-Houston, D.: Controls on land surface temperature in deserts of southern
938 California derived from MODIS satellite time series analysis, 2000 to 2018. *Climate*, 7, 32,
939 <https://doi.org/10.3390/cli7020032>, 2019.

940 Querol, X.: The Occurrence and Distribution of Trace Elements in the Teruel Mining District Coals and
941 their Behaviour during Coal Combustion. European Coal and Steel Community Project
942 7220/ED/014, 1993.

943 Querol, X., Whateley, M.K.G., Fernandez-Turiel, J.L., Tuncali, E.: Geological controls on the mineralogy
944 and geochemistry of the Bey pazari lignite, Central Anatolia, Turkey. *Int. J. Coal. Geol.*, 33:255–
945 271, 1997.

946 Raupach, M.R., Gillette, D.A., Leys, J.F.: The effect of roughness elements on wind erosion threshold.
947 *J. Geophys. Res.*, 98, 3023-3029, 1993.

948 [Reheis, M.C., Goodmacher, J.C., Harden, J.W., McFadden, L.D., Rockwell, T.K., Shroba, R.R., Sowers,](#)
949 [J.M. and Taylor, E.M. Quaternary soils and dust deposition in southern Nevada and California.](#)
950 [Geological Society of America Bulletin, 107\(9\), pp.1003-1022, 1995.](#)

951 [Reheis, M.C. and Kihl, R. Dust deposition in southern Nevada and California, 1984–1989: Relations to](#)
952 [climate, source area, and source lithology. Journal of Geophysical Research: Atmospheres,](#)
953 [100\(D5\), pp.8893-8918, 1995.](#)

954 [Reheis, M.C. Dust deposition downwind of Owens \(dry\) Lake, 1991–1994: Preliminary findings. Journal](#)
955 [of Geophysical Research: Atmospheres, 102\(D22\), pp.25999-26008, 1997.](#)

956 [Reheis, M.C., Budahn, J.R. and Lamothe, P.J. Geochemical evidence for diversity of dust sources in the](#)
957 [southwestern United States. Geochimica et Cosmochimica Acta, 66\(9\), pp.1569-1587, 2002.](#)

958 [Reheis, M.C., Budahn, J.R., Lamothe, P.J. and Reynolds, R.L. Compositions of modern dust and surface](#)
959 [sediments in the Desert Southwest, United States. Journal of Geophysical Research: Earth](#)
960 [Surface, 114\(F1\), 2009.](#)

961 Reheis, M.C., Bright, J., Lund, S.P., Miller, D.M., Skipp, G., Fleck, R.J.: A half-million-year record of
962 paleoclimate from the Lake Manix core, Mojave Desert, California. *Palaeogeogr., Palaeoclim.*
963 *Palaeoecol.*, 365–366, pp. 11-37, 2012.

964 [Reynolds, R.L., Reheis, M., Yount, J. and Lamothe, P. Composition of aeolian dust in natural traps on](#)
965 [isolated surfaces of the central Mojave Desert—Insights to mixing, sources, and nutrient](#)
966 [inputs. Journal of Arid Environments, 66\(1\), pp.42-61, 2006.](#)

967 [Reynolds, R.L., Yount, J.C., Reheis, M., Goldstein, H., Chavez Jr, P., Fulton, R., Whitney, J., Fuller, C. and](#)
968 [Forester, R.M. Dust emission from wet and dry playas in the Mojave Desert, USA. Earth Surface](#)
969 [Processes and Landforms: The Journal of the British Geomorphological Research Group,](#)
970 [32\(12\), pp.1811-1827, 2007.](#)

971 Reynolds, R.L., Bogle, R., Vogel, J., Goldstein, H., Yount, J.: Dust emission at Franklin Lake Playa, Mojave
972 Desert (USA): Response to meteorological and hydrologic changes 2005–2008, in: Oren, A.,
973 Naftz, D. L., Wurtsbaugh, W. A. (Eds.), *Saline lakes around the world: unique systems with*
974 *unique values*, *Natural Resources and Environmental Issues* 15, 105–116,
975 <https://digitalcommons.usu.edu/nrei/vol15/iss1/18> (last access: 7 November 2023), 2009.

976 Rietveld, H.M.: A profile refinement method for nuclear and magnetic structures. *Journal of Applied*
977 *Crystallography* 2, 65–71, 1969.

978 [Scanza, R. A., Mahowald, N., Ghan, S., Zender, C. S., Kok, J. F., Liu, X., ... & Albani, S. \(2015\). Modeling](#)
979 [dust as component minerals in the Community Atmosphere Model: development of](#)
980 [framework and impact on radiative forcing. Atmospheric Chemistry and Physics, 15\(1\), 537-](#)
981 [561.](#)

982 Scarlett, N. & Madsen, I.: Quantification of phases with partial or no known crystal structures. *Powder*
983 *Diffraction*, 21(4), 278-284, 2006.

984 Shao, Y., Raupach, M.R., & Findlater, P.A.: Effect of saltation bombardment on the entrainment of dust
985 by wind. *Journal of Geophysical Research: Atmospheres*, 98(D7), 12719-12726, 1993.

986 [Shao, Y. \(2001\). A model for mineral dust emission. Journal of Geophysical Research: Atmospheres,](#)
987 [106\(D17\), 20239-20254.](#)

988 [Shao, Y., Wyrwoll, K. H., Chappell, A., Huang, J., Lin, Z., McTainsh, G. H., ... & Yoon, S. \(2011\). Dust](#)
989 [cycle: An emerging core theme in Earth system science. Aeolian Research, 2\(4\), 181-204.](#)

990 Shi, Z.B., Krom, M.D., Bonneville, S.: Formation of Iron Nanoparticles and Increase in Iron Reactivity in
991 Mineral Dust during Simulated Cloud Processing. *Environ. Sci. Technol.* 43, 6592-6596, 2009.

- 992 Sperazza, M., Moore, J.N., Hendrix, M.: High-Resolution particle size analysis of naturally occurring
 993 very fine-grained sediment through laser diffractometry. *J. Sediment. Res.*, 74 (5), 736-743,
 994 2004.
- 995 [Stout, J. E., & Lee, J. A. \(2003\). Indirect evidence of wind erosion trends on the Southern High Plains](#)
 996 [of North America. *Journal of Arid Environments*, 55\(1\), 43-61.](#)
- 997 Sullivan, R.C., Guazzotti, S.A., Sodeman, D.A., Tang, Y., Carmichael, G.R., & Prather, K.A.: Mineral dust
 998 is a sink for chlorine in the marine boundary layer. *Atmospheric Environment*, 41(34), 7166–
 999 7179, 2007.
- 1000 Thorez, J.: Practical Identification of Clay Minerals: A Handbook for Teachers and Students in Clay
 1001 Mineralogy. Institute of mineralogy, Liège State University, Belgium, Lelotte Eds, B 4820
 1002 DISON (Belgique),90pg, 1976.
- 1003 Tong, D.Q., Dan, M., Wang, T., Lee, P.: Long-term dust climatology in the western United States
 1004 reconstructed from routine aerosol ground monitoring, *Atmos. Chem. Phys.*, 12, 5189–5205,
 1005 <https://doi.org/10.5194/acp-12-5189-2012>, 2012.
- 1006 TOPAS: TOPAS and TOPAS-Academic: an optimization program integrating computer algebra and
 1007 crystallographic objects written in C++. *J. Appl. Cryst.* (2018). 51, 210-218, 2018.
- 1008 Urban, F.E., Reynolds, R.L., Fulton, R.: The dynamic interaction of climate, vegetation, and dust
 1009 emission, Mojave Desert, USA. A. Fernandez-Bernal, M.A. De La Rosa (Eds.), *Arid*
 1010 *Environments and Wind Erosion*, NOVA Science Publishers, Inc., pp. 243-267, 2009.
- 1011 Urban, F.E., Goldstein, H.L., Fulton, R., Reynolds, R.L.: Unseen dust emission and global dust
 1012 abundance: documenting dust emission from the Mojave Desert (USA) by daily remote
 1013 camera imagery and wind-erosion measurements. *J. Geophys. Res. Atmos.*, 123 (16), pp.
 1014 8735-8753, 2018.
- 1015 USGS, U. S. Geological Survey Open-File Report 01-041. A Laboratory Manual for X-Ray Powder
 1016 Diffraction <https://pubs.usgs.gov/of/2001/of01-041/htmldocs/methods/oamount.htm>. Last
 1017 access: 17th January of 2024.
- 1018 [Vandenbergh, R. E., Barrero, C. A., Da Costa, G. M., Van San, E., and De Grave, E.: Mössbauer](#)
 1019 [characterization of iron oxides and \(oxy\) hydroxides: the present state of the art. *Hyperfine*](#)
 1020 [Interactions](#), 126, 247-259, 2000.
- 1021 Weaver, C., Ginoux, P., Hsu, N., Chou, M.-D., Joiner, J.: Radiative forcing of Saharan dust: GOCART
 1022 model simulations compared with ERBE data. *J. Atmos. Sci.*, 59, 736-747, 2002.
- 1023 Whitney, J.W., Breit, G.N., Buckingham, S.E., Reynolds, R.L., Bogle, R.C., Luo, L., Goldstein, H.L., Vogel,
 1024 J.M.: Aeolian responses to climate variability during the past century on Mesquite Lake Playa,
 1025 Mojave Desert. *Geomorphology*, 230, 13-25, 2015.
- 1026 Young, R.A.: The Rietveld method. International Union of Crystallography. Oxford University Press, UK,
 1027 1993.
- 1028 Zubko, N., Munoz, O., Zubko, E., Gritsevich, M., Escobar-Cerezo, J., Berg, M. J. and Peltoniemi, J.: Light
 1029 scattering from volcanic-sand particles in deposited and aerosol form. *Atmospheric*
 1030 *Environment*, 215, 116813. <https://doi.org/10.1016/j.atmosenv.2019.06.051>, 2019.

1031 **Figure captions:**

1032 **Figure 1:** Study area map including the playa lakes studied together with a geologic map, simplified
 1033 from Jennings et al. (1962) and Miller et al. (2014). The star represents the Zzyzx complex [and green](#)
 1034 [dots the samples used in this study](#). Basemap: Imagery data from © Google Earth Pro v: 7.3.6.9345.

1035 **Figure 2:** Map of Frequency of Occurrence (FoO) of dust optical depth > 0.1 over the study region
1036 derived from MODIS C6.1 Aqua (1:30PM equatorial passing time) Level 2 Deep Blue aerosol products
1037 at 0.1 degree resolution. A dust occurrence is counted when ~~AOD-DOD~~ > 0.1, Angstrom Exponent <
1038 0.3 and ~~AOD-DOD~~ at 412 nm > ~~AOD-DOD~~ at 470 nm. Blue iso-contours represent 2, 5 and 10 % of daily
1039 occurrences per year averaged over 20 years (2003-2022). Green dots represent the samples collected
1040 and used in this study. Basemap: Imagery data from © Google Earth Pro v: 7.3.6.9345.

1041 **Figure 3:** EMIT scenes emit20231015T215209_color-visRGB and emit20230728T214142_color-visRGB
1042 at 60 m per pixel showing the diversity of Fe²⁺, Fe³⁺ and Fe²⁺ and Fe³⁺ bearing minerals and the
1043 carbonates, salt and phyllosilicates minerals.

1044 **Figure 4:** Examples of samples collected in the Mojave Desert including crusts (a), aeolian ripples (b),
1045 massive compact crust (c) and a salty spongy crust (d).

1046 **Figure 5:** Fully dispersed particle size distribution (FDPD) and minimally dispersed particle size
1047 distribution (MDPSD) for crusts and aeolian ripples from the Mojave Desert (median PSD from all the
1048 samples), Soda, Mesquite, Cronese, Ivanpah and Coyote Lakes. In shaded blue and brown the standard
1049 deviation of each PSD (n° of samples used in Table 1), except for Ivanpah and Coyote Lakes (only 1
1050 sample each).

1051 Figure 6: % of mass fractions from the dry sieved size fractions (250-50, 80-250, 63-80, 40-63, 20-40
1052 and <20 µm). The range of the enrichment factors of each mineral group for each dry size fraction of
1053 the 16 crust samples (blue) and for the 4 aeolian ripples samples (red).

1054 **Figure 67:** Box-plot showing averaged mineral contents for all samples, crusts and aeolian ripples (wt
1055 %).

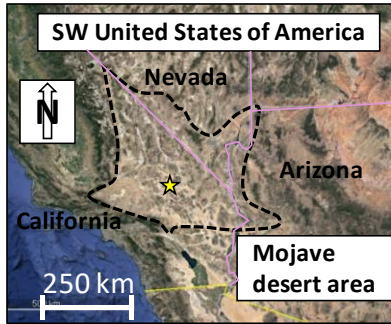
1056 **Figure 78:** Geological cross section and mineralogy of the crusts of the Soda Lake. Top panel represent
1057 major mineralogy composition. Mid panel represents the position of the samples, the Zzyzx complex,
1058 and the path of the cross section. Bottom schematic cross section simplifying the position in the basin.
1059 Basemap: Imagery data from © Google Earth Pro v: 7.3.6.9345.

1060 **Figure 89:** Cross-correlation plots of the clay contents and amphibole with the FeT (a) and clay
1061 minerals and FeA (b), all in wt % in crusts.

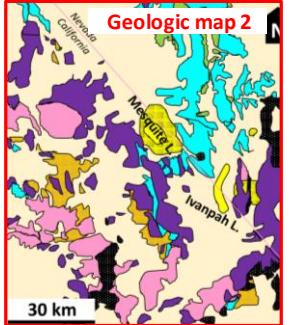
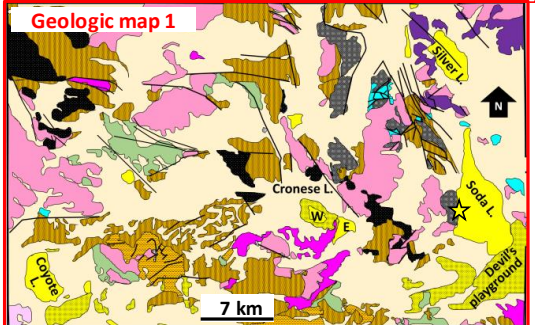
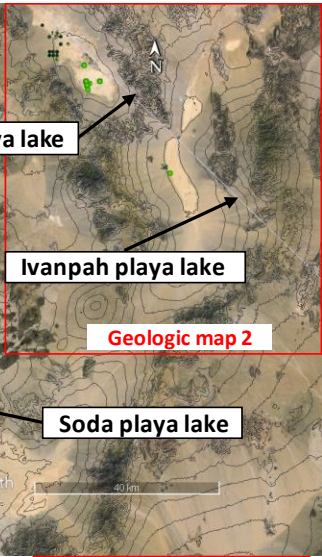
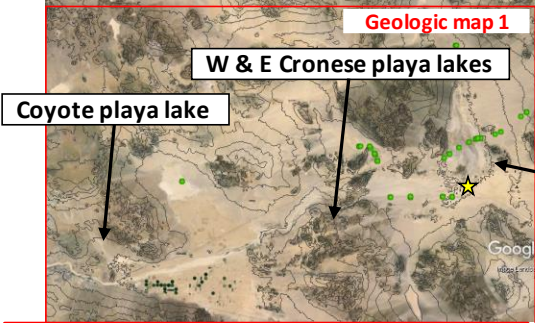
1062 **Figure 910:** ~~Fe mode of occurrence~~ Modes of occurrences of Fe comparison between the crusts (C)
1063 playa lakes analysed in this study, the average of the crusts and ripples (R) at Mojave Desert, Morocco
1064 and Iceland Top surface (TS). FeA is referred to the exchangeable Fe and nano Fe oxides, FeD is the Fe
1065 content in hematite and goethite, FeM is the Fe content in maghemite/magnetite and FeS is the Fe
1066 content in Fe bearing minerals.

1067 **Figure 1011:** Conceptual model of wet and dry playa lakes differences due to groundwater differences
1068 and how this can affect the mineralogy of the surface in the playa lakes. Also illustrated is the expected
1069 dust emission rate, major mineralogy and modes of Fe mode of occurrence occurrences of Fe
1070 differences expected in the emitted dust.

1071
1072 Figure 1.



Google Earth
 Image Landsat / Copernicus
 Data LDEO-Columbia, NSF, NOAA
 Data SIO, NOAA, U.S. Navy NGA, GEBCO



SEDIMENTARY & METAMORPHIC

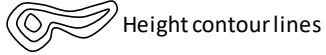
- Aluvial sediments
- Lake sediments
- Dune sands
- Plio-Pleistocene sediments
- Miocene sediments
- Mesozoic metamorphics
- Pleozoic mostly limestones & dolostones
- Cambrian & Precambrian metamorphics

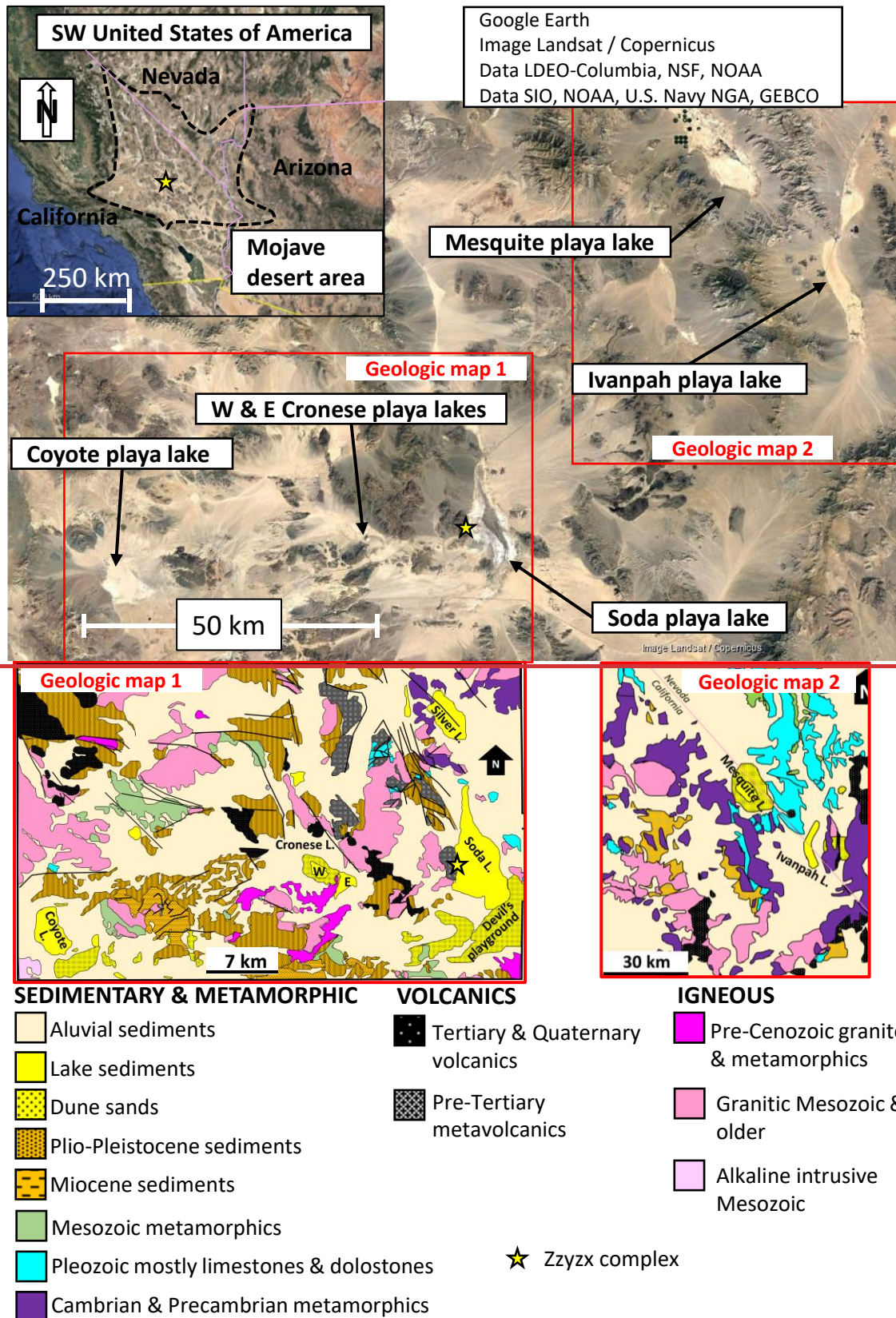
VOLCANICS

- Tertiary & Quaternary volcanics
- Pre-Tertiary metavolcanics

IGNEOUS

- Pre-Cenozoic granite & metamorphics
- Granitic Mesozoic & older
- Alkaline intrusive Mesozoic
- Zzyzx complex
- Samples

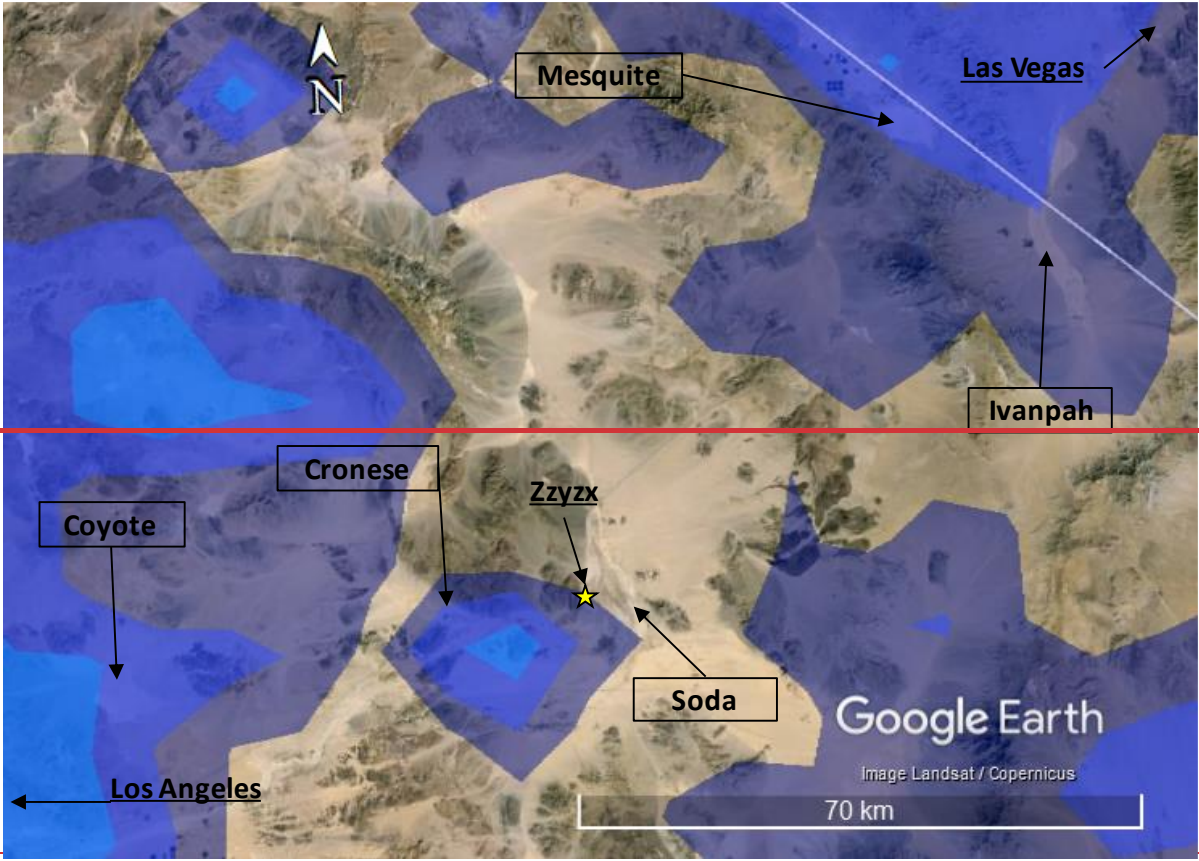




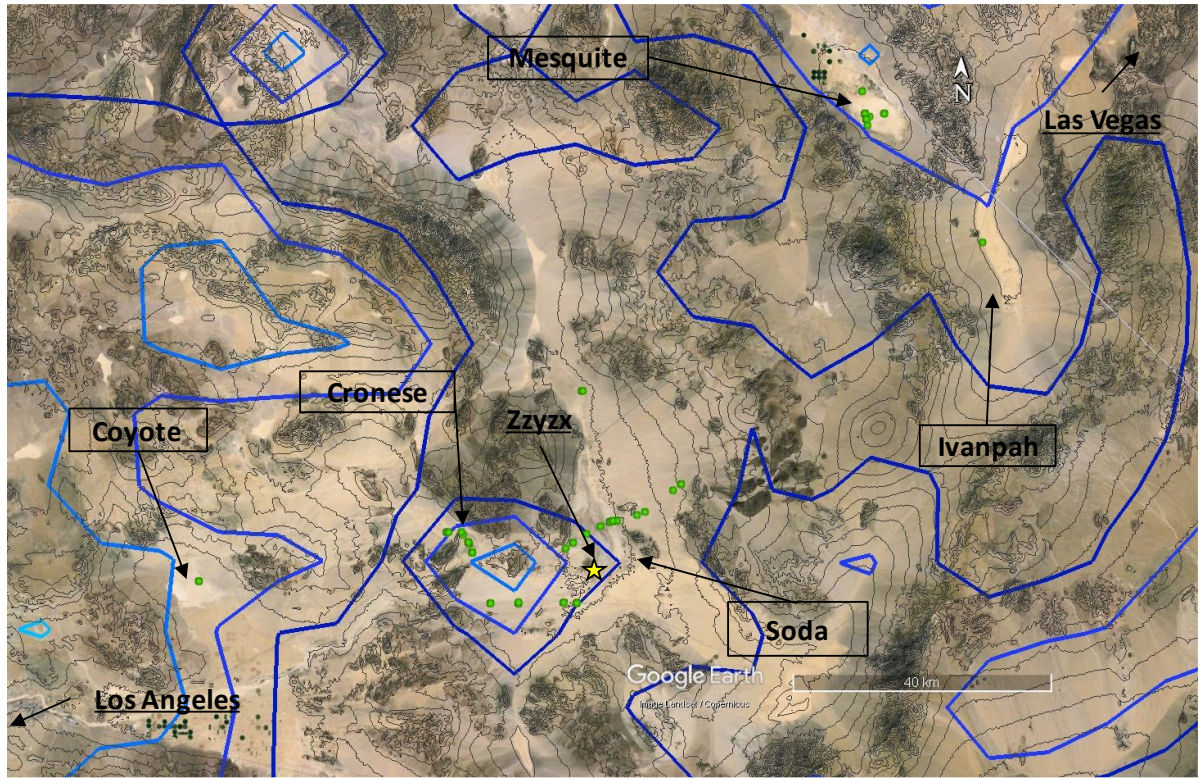
1074

1075

1076 Figure 2.



1077



1078

1079

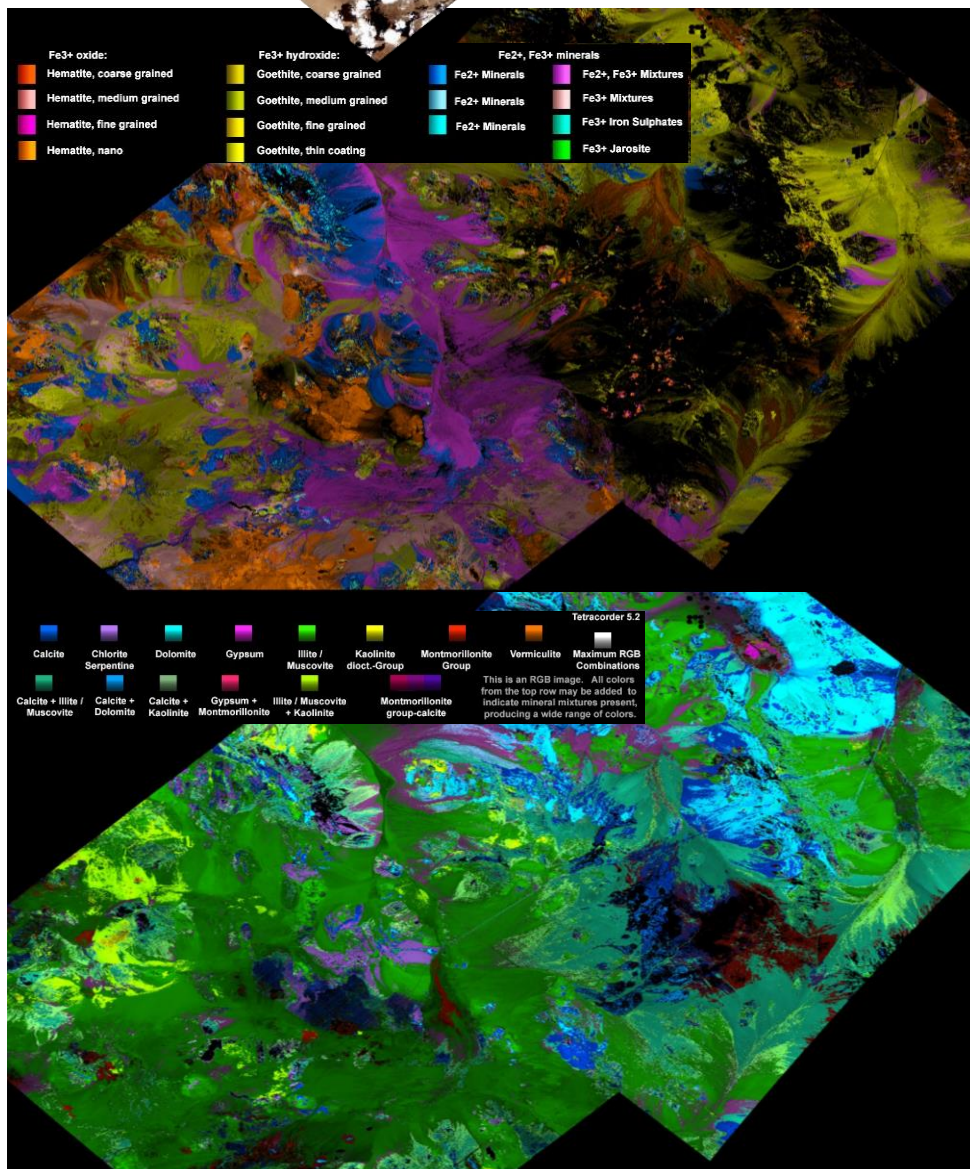
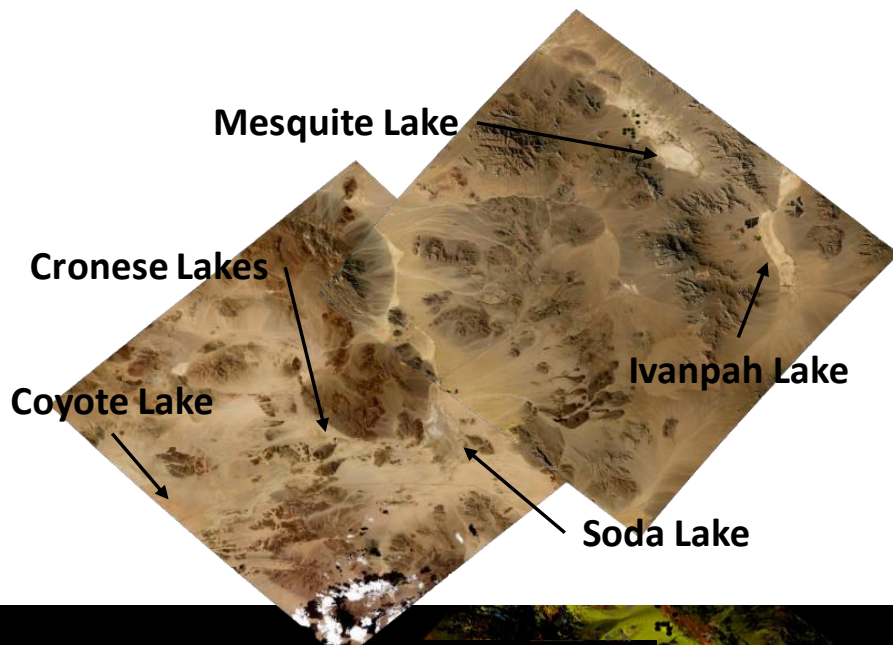
1080

1081

1082

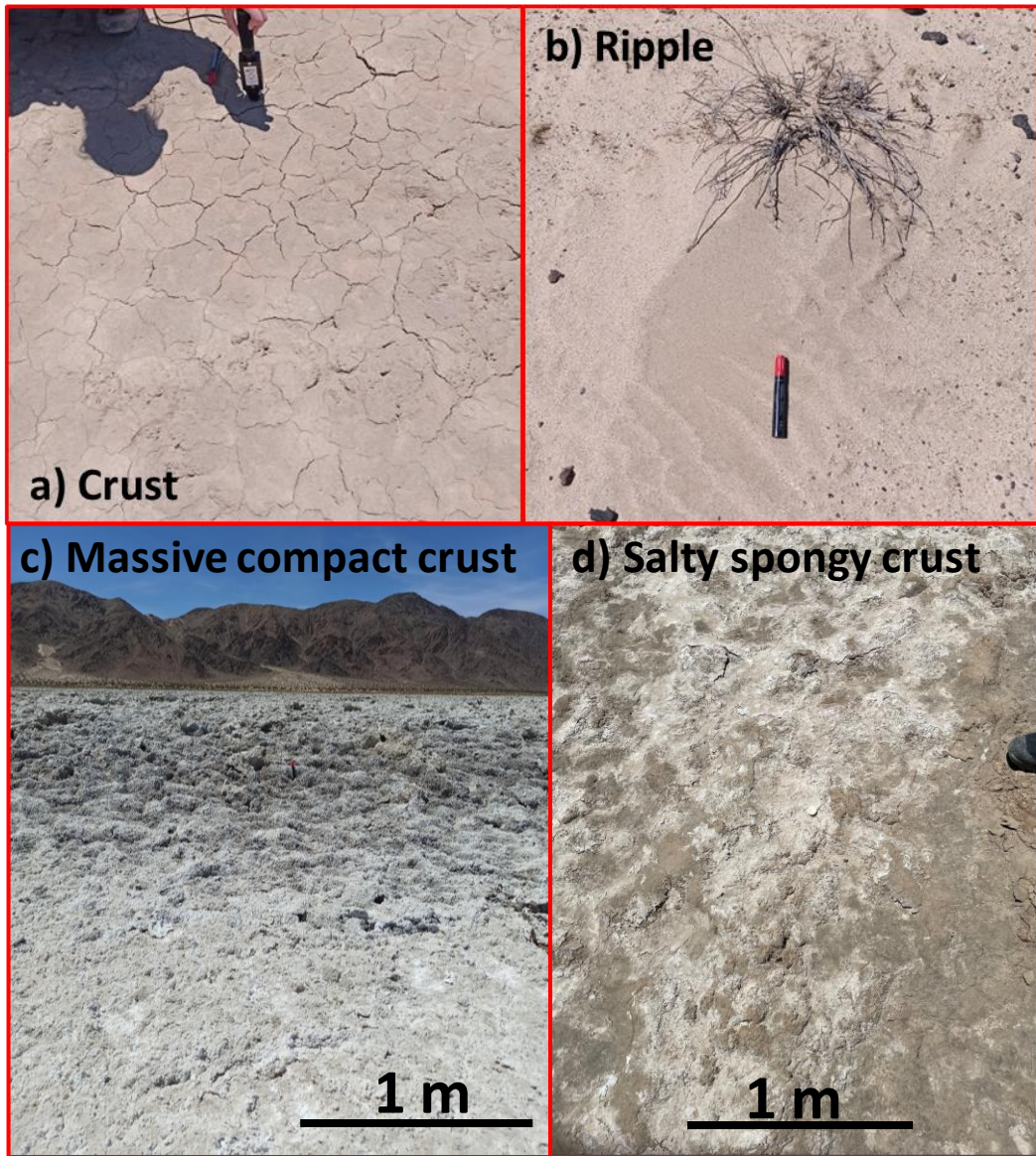
1083
1084
1085
1086
1087
1088
1089
1090
1091
1092
1093
1094
1095
1096
1097
1098
1099
1100
1101

Figure 3.



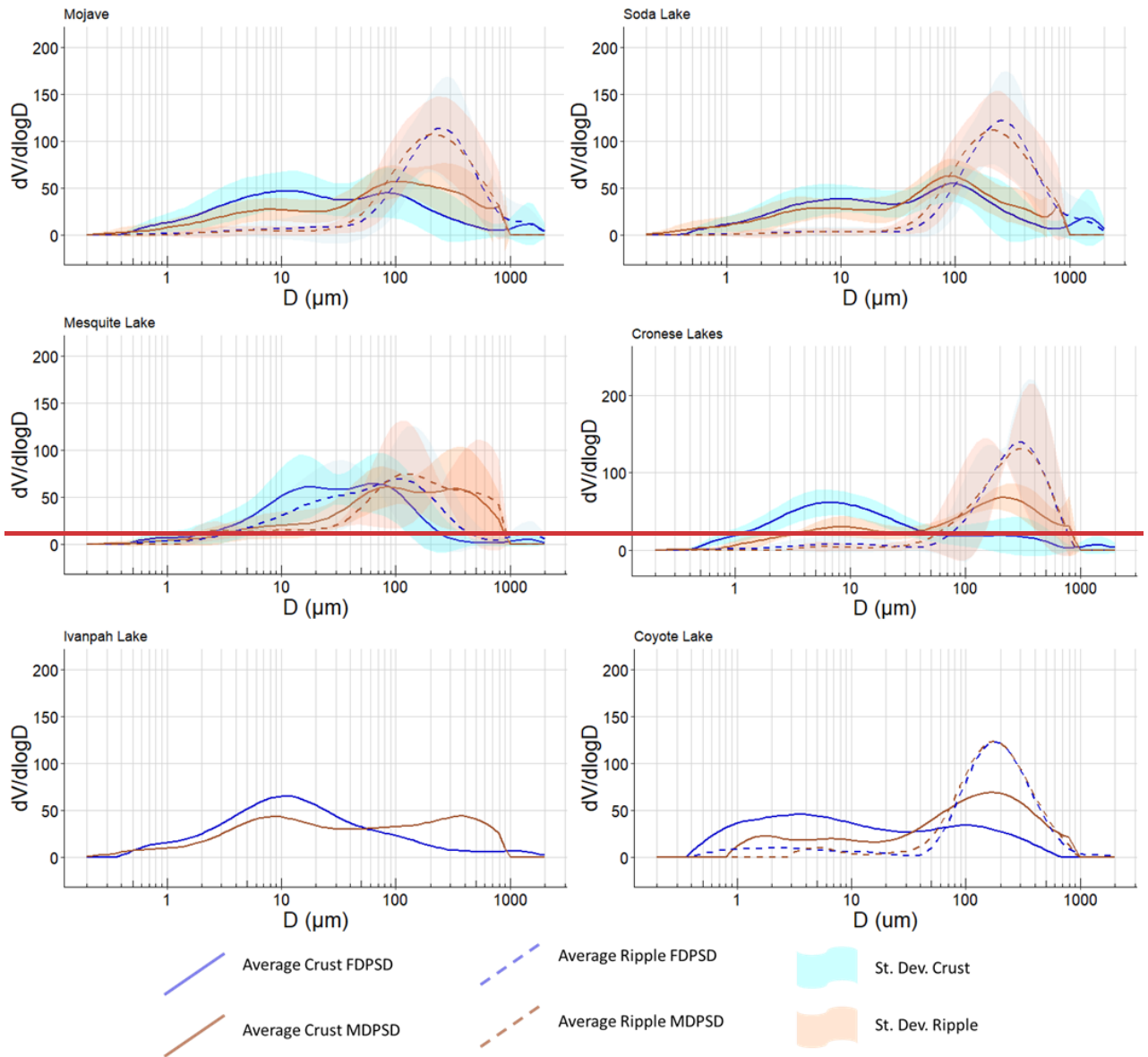
1102

1103 Figure 4.

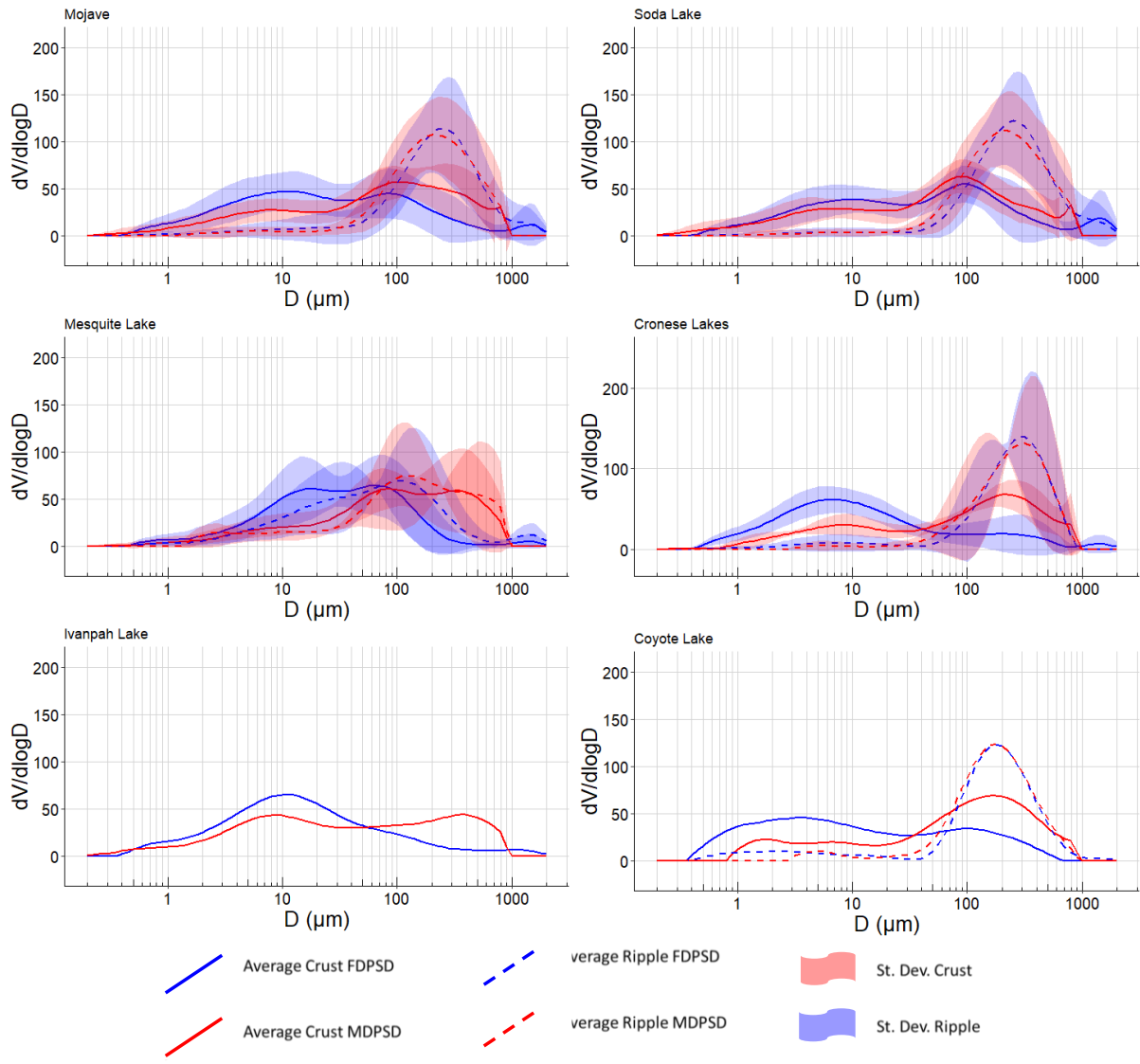


1104
1105
1106
1107
1108
1109
1110
1111
1112
1113
1114
1115
1116
1117
1118
1119

Figure 5.



1120



1121

1122

1123

1124

1125

1126

1127

1128

1129

1130

1131

1132

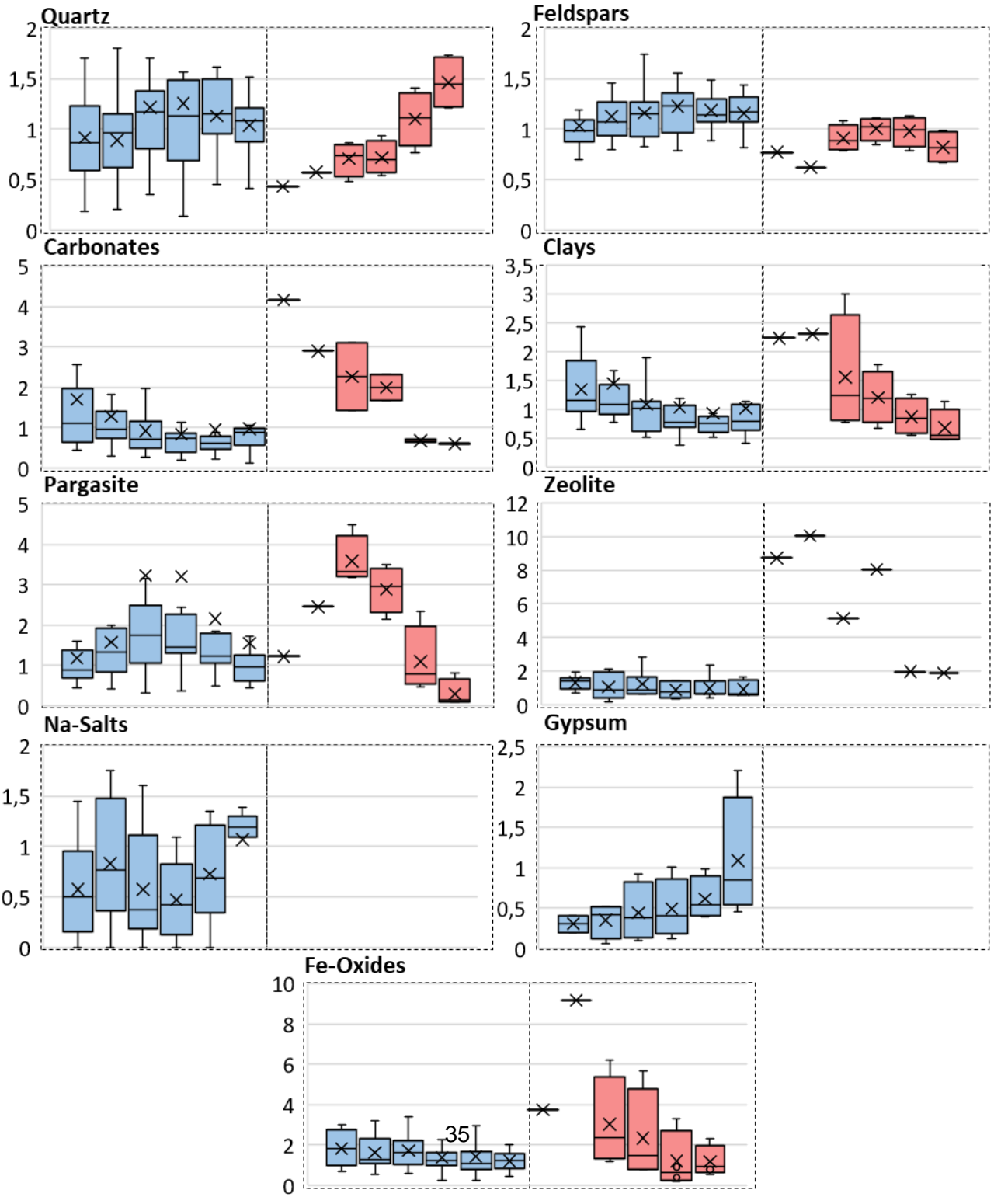
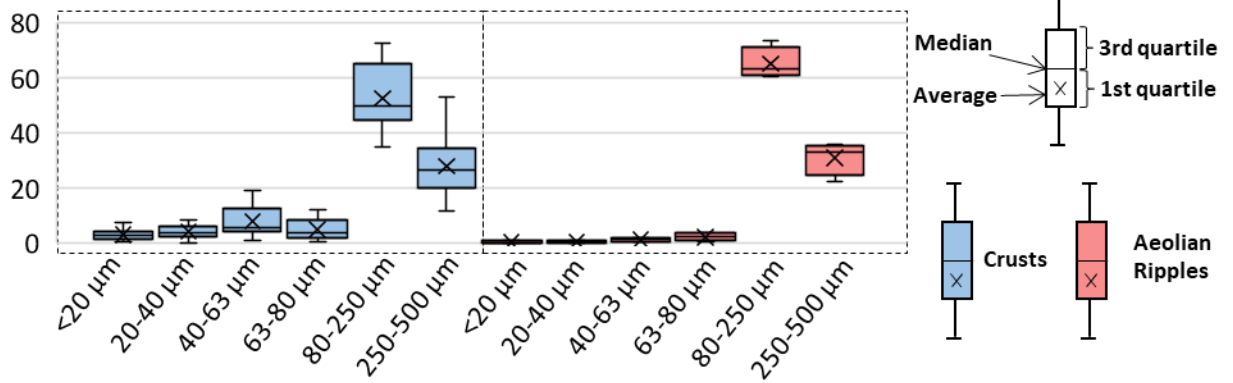
1133

1134

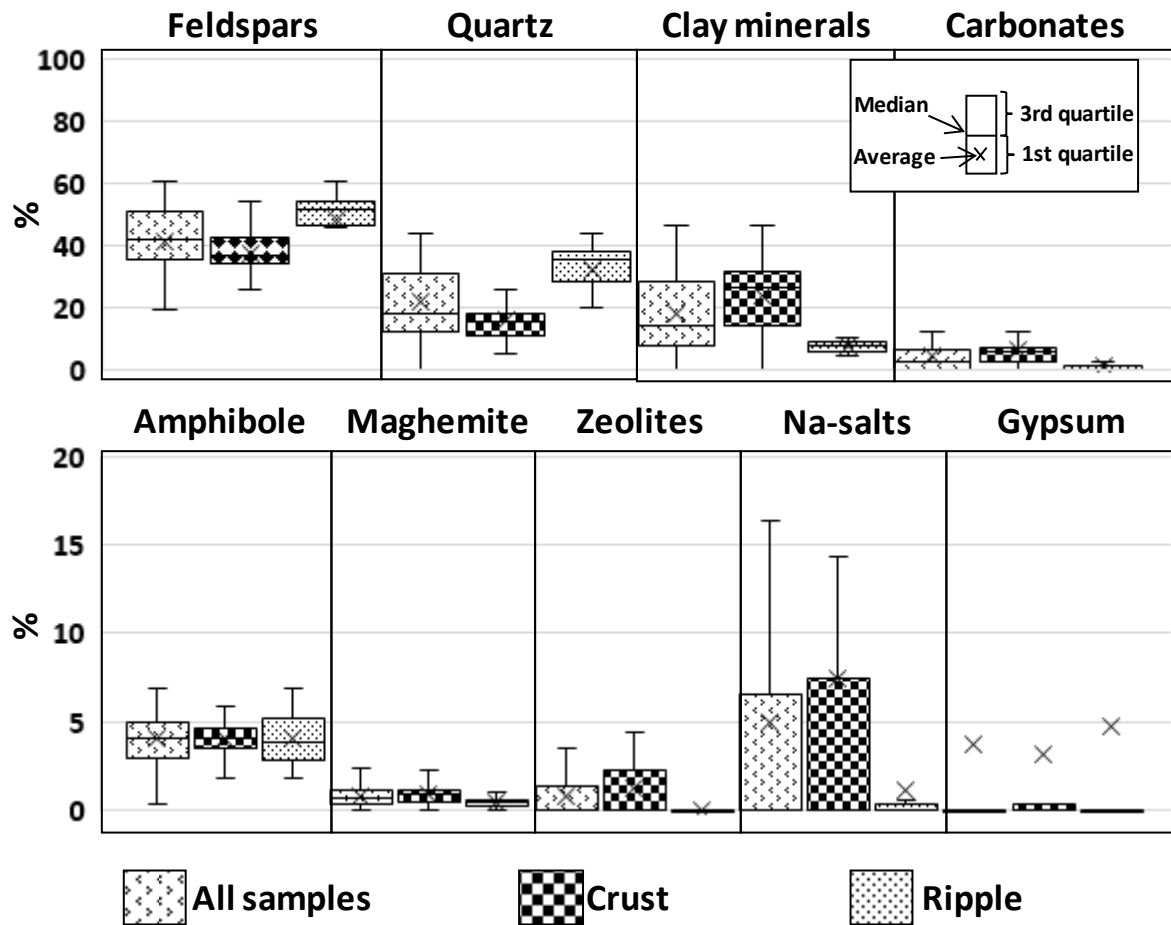
1135

Figure 6.

% of mass fraction



1137 Figure 7.



1138

1139

1140

1141

1142

1143

1144

1145

1146

1147

1148

1149

1150

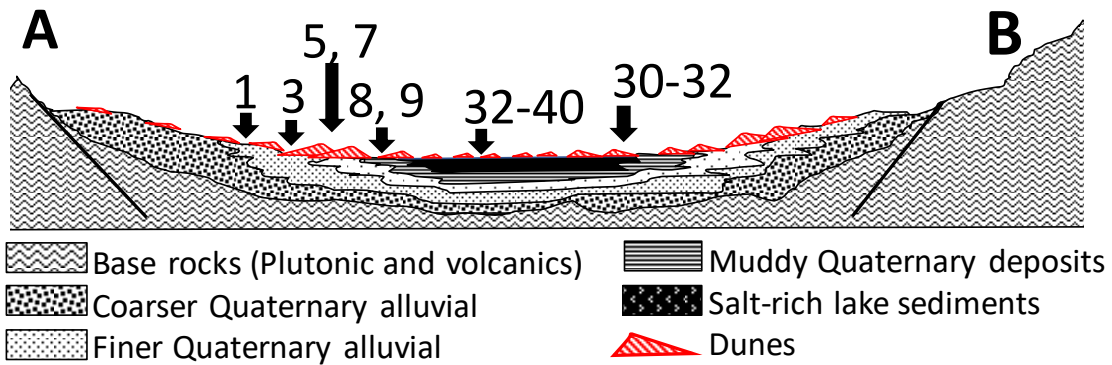
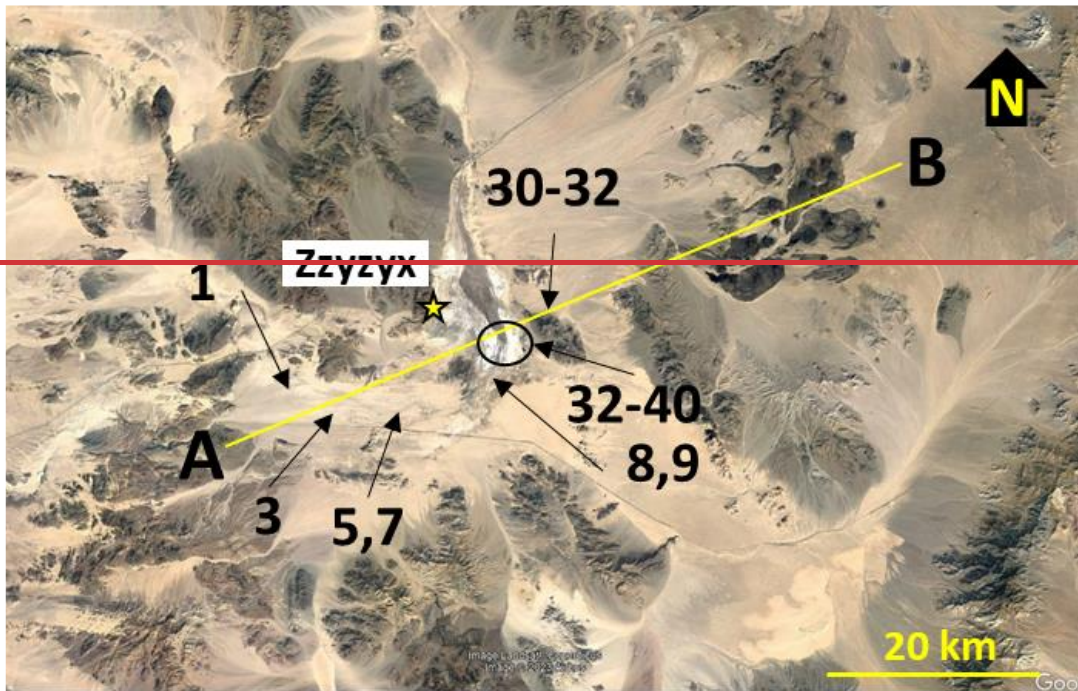
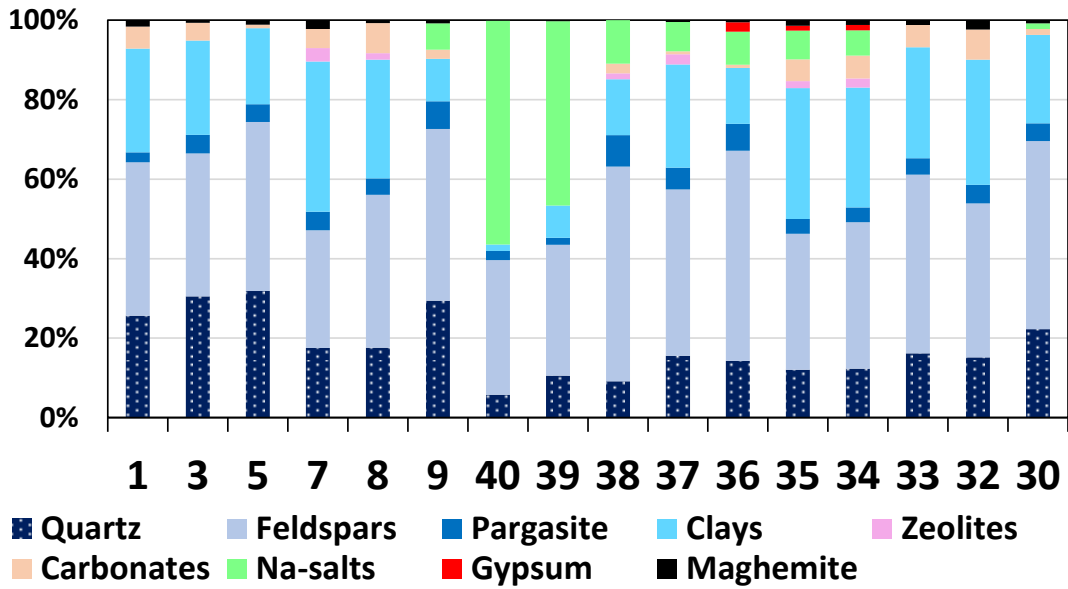
1151

1152

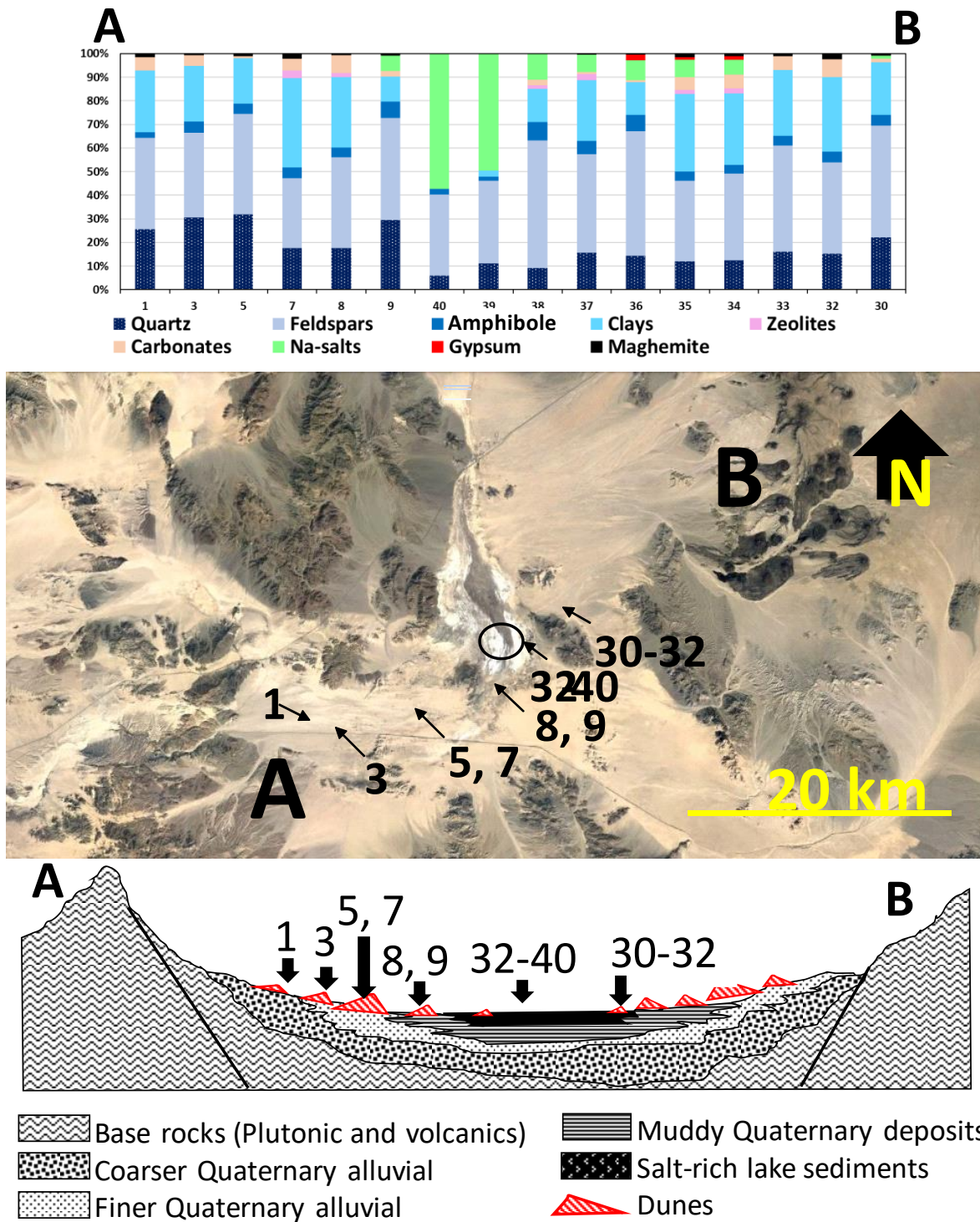
1153

1154

1155 Figure 87.



1156

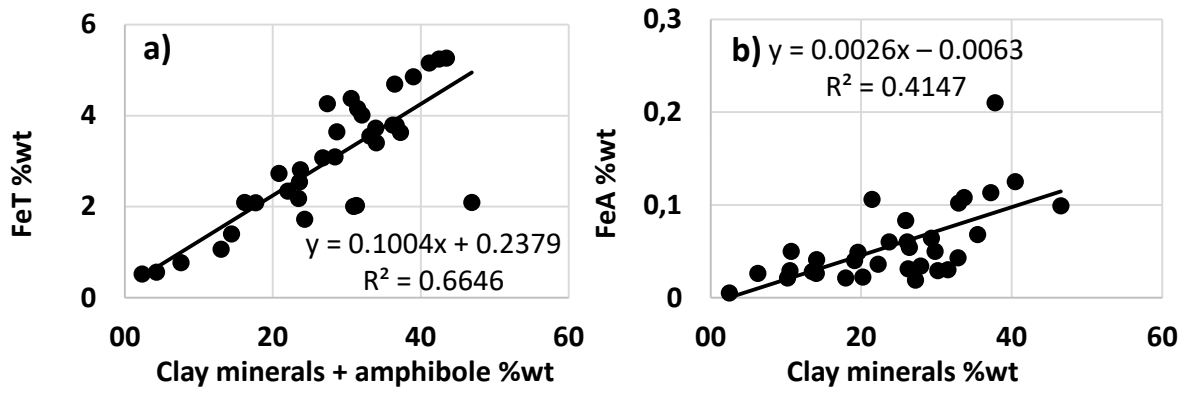


1157

1158

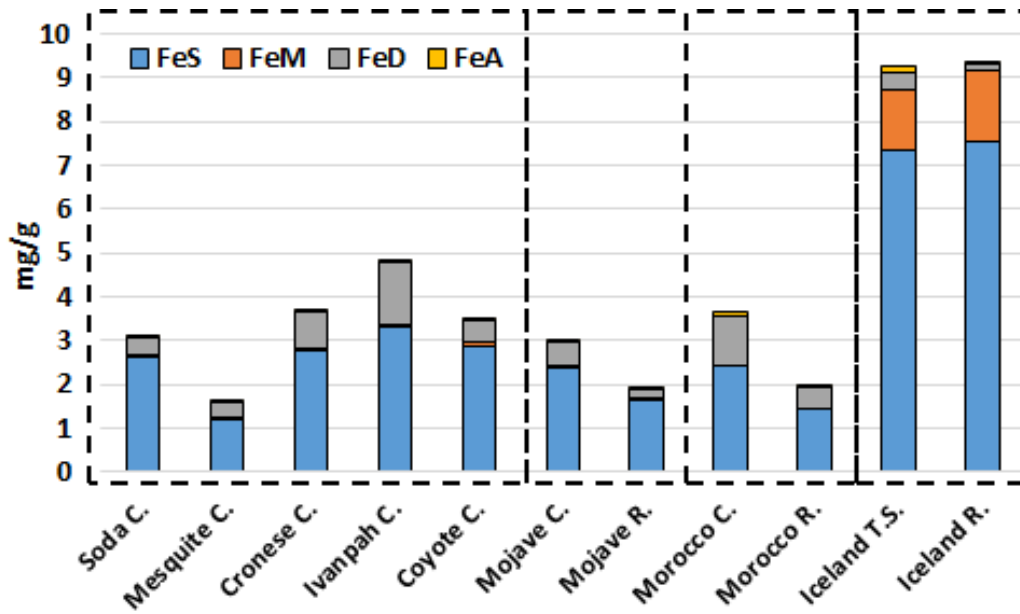
1159

Figure 89.



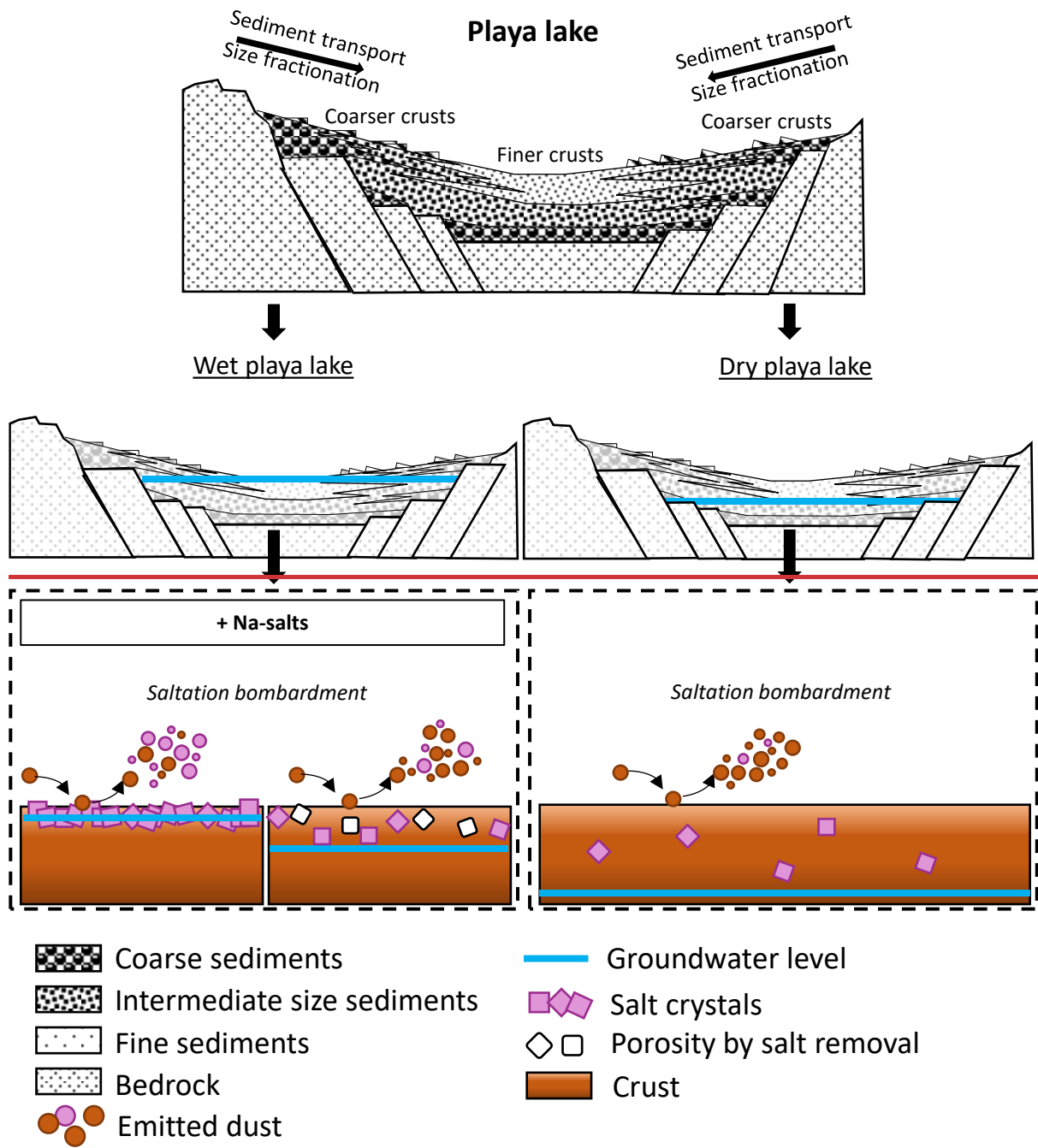
1160
 1161
 1162
 1163
 1164
 1165
 1166
 1167
 1168
 1169
 1170
 1171
 1172
 1173
 1174
 1175
 1176
 1177
 1178
 1179
 1180
 1181

1182 Figure 910.

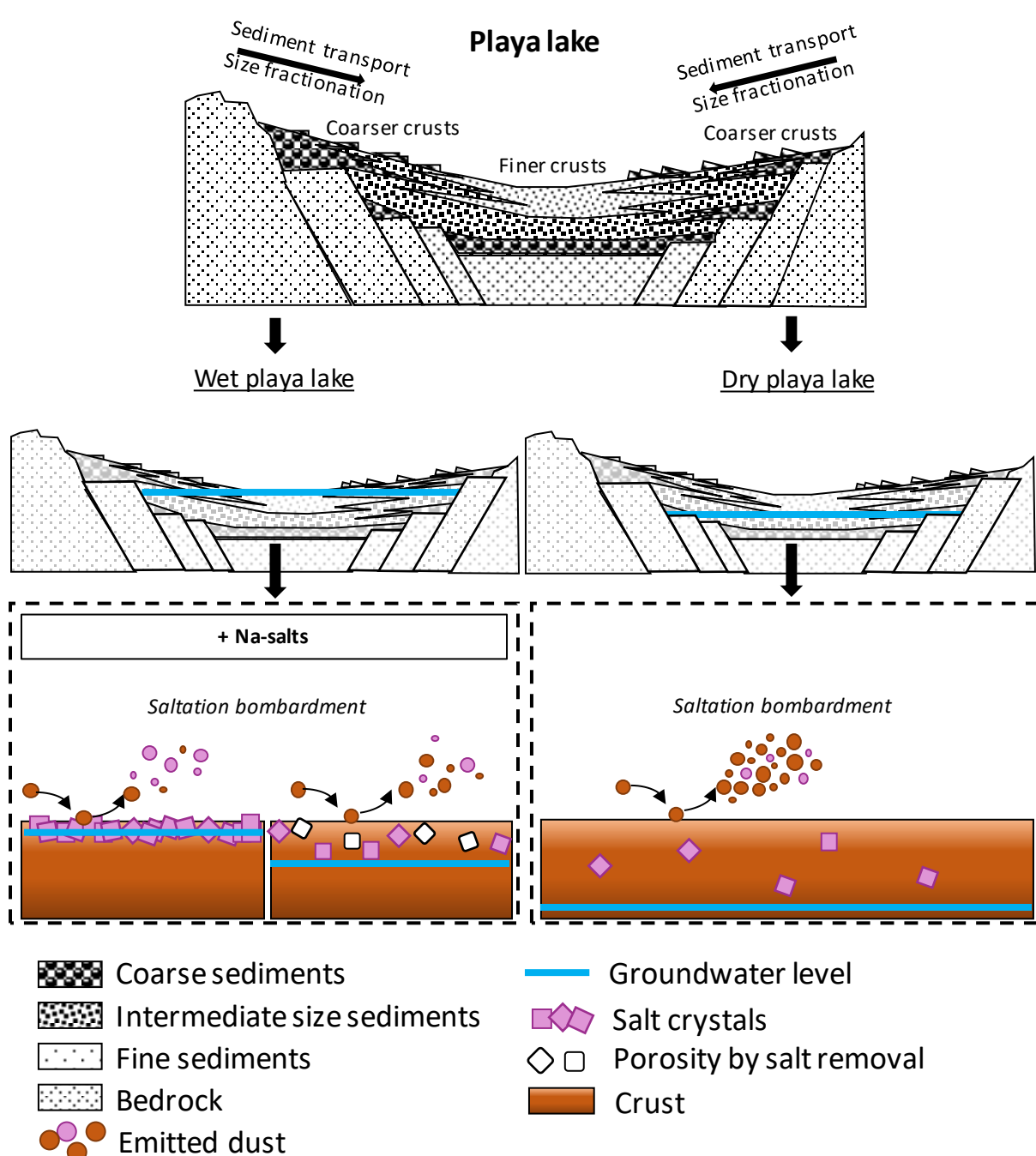


1183
 1184
 1185
 1186
 1187
 1188
 1189
 1190
 1191
 1192
 1193
 1194
 1195
 1196
 1197
 1198
 1199
 1200
 1201
 1202
 1203

Figure 1011.



1204



1205
 1206
 1207
 1208
 1209
 1210
 1211
 1212
 1213
 1214

1215 Table 1. Full range (<2000 μm), <63μm and >63 to 2000 μm mean diameter, standard deviation, min.,
 1216 and max for minimally dispersed particle size distribution (MDPSD) and fully dispersed particle size
 1217 distribution (FDPSD).

Surface	Location	N	MDPSD		
			Full range	≤ 63 μm	>63 to 2000 μm
			Mean of medians ± Std. Dev. [Min,Max]		
Crusts	Mojave	35	92 ± 74 [10,349]	22 ± 6.4 [11,34]	254 ± 71 [155,489]
Ripples		20	226 ± 88 [88, 418]	37 ± 6.0 [20,46]	276 ± 80 [130,424]
Crusts	Soda	17	63 ± 47 [10,156]	21 ± 6.5 [11,31]	234 ± 82 [155,489]
	Cronese	9	109 ± 60 [35,195]	18 ± 2.2 [15,22]	280 ± 40 [238,357]
	Mesquite	7	141 ± 117 [31,349]	28 ± 5.6 [21,34]	257 ± 79 [157,387]
	Ivanpah	1	35 ± NA [35,35]	16 ± NA [16,16]	314 ± NA [314,314]
	Coyote	1	101 ± NA [101,101]	20 ± NA [20,20]	254 ± NA [254,254]
Ripples	Soda	15	231 ± 87 [88,418]	39 ± 3.5 [29,43]	275 ± 77 [130,424]
	Cronese	2	264 ± 147 [160,368]	40 ± 8.8 [34,46]	292 ± 120 [208,377]
	Mesquite	2	167 ± 112 [110,225]	26 ± 8.9 [20,32]	286 ± 146 [183,389]
	Ivanpah	0	NA	NA	NA
	Coyote	1	179 ± NA [179,179]	32 ± NA [32,32]	236 ± NA [236,236]
			FDPSD		
Surface	Location	N	FDPSD		
			Full range	≤ 63 μm	>63 to 2000 μm
			Mean of medians ± Std. Dev. [Min,Max]		
Crusts	Mojave	35	37 ± 48 [4.9,240]	18 ± 6.6 [8.4,35]	306 ± 237 [106,1093]
Ripples		20	213 ± 92 [28,362]	29 ± 8.3 [15,48]	335 ± 99 [213,561]
Crusts	Soda	17	52 ± 61 [8.4,240]	19 ± 5.3 [12,27]	321 ± 212 [113,815]
	Cronese	9	17 ± 23 [4.9,77]	12 ± 3.1 [8.4,19]	381 ± 345 [144,1093]
	Mesquite	7	34 ± 28 [11,91]	24 ± 7.7 [16,35]	185 ± 104 [106,336]
	Ivanpah	1	12 ± NA [21,21]	15 ± NA [15,15]	347 ± NA [347,347]
	Coyote	1	8.4 ± NA [8.4,8.4]	12 ± NA [12,12]	187 ± NA [187,187]
Ripples	Soda	15	234 ± 82 [92,362]	31 ± 7.9 [21,48]	346 ± 97 [238,561]
	Cronese	2	236 ± 126 [147,325]	18 ± NA [18,18]	295 ± 108 [219,371]
	Mesquite	2	67 ± 56 [28,107]	27 ± 3.5 [24,29]	336 ± 173 [213,458]
	Ivanpah	0	NA	NA	NA
	Coyote	1	156 ± NA [156,156]	15 ± NA [15,15]	245 ± NA [245,245]

1218
 1219
 1220
 1221
 1222
 1223
 1224
 1225
 1226
 1227

1228 Table 2. Average and standard deviations of the mineral contents (wt %) from crust and aeolian ripple
 1229 samples from the Mojave Desert and the different study basins. NaN, not a number. Maghemite is
 1230 considered as Maghemite and Magnetite

	Clays	Carbonate	Salts	Zeolites	Maghemite	Quartz	Feldspars	Gypsum	Amphibole
CRUSTS	24±11	6.6±6.6	7.3±13	1.2±1.9	0.92±0.59	16±7.2	37±9.7	3.1±14	4.1±1.5
Soda	22±11	3.6±2.6	8.9±17	0.77±1.1	0.97±0.66	18±7.7	40±6.7	0.29±0.68	4.5±1.6
Cronese	31±11	5.4±1.8	2.2±3.4	2.4±1.7	1.0±0.28	14±7.3	40±5.5	<0.1	3.4±1.5
Coyote	28	7,2	1,2	8,5	0,48	11	37	<0.1	5.6
Ivanpah	36	6.9	<0.1	<0.1	1,2	15	36	<0.1	3.5
Mesquite	17±8.2	15±11	12±14	<0.1	0.71±0.75	14±5.8	24±12	15±29	2.8±1.4
RIPPLES	7.8±2.3	1.1±2.2	1.1±3,7	0.12±0.52	0.49±0.28	32±9.5	48±13	4.7±20	4.1±1.6
Soda	7.4±1.8	0.47±0.73	0.19±0.46	<0.1	0.49±0.25	35±4.5	52±4.7	<0.1	4.3±1.5
Cronese	8.4±0.60	1.2±1.7	<0.1	<0.1	0.83±0.33	32±9.0	53±0.03	<0.1	4.7±3.2
Coyote	7.9	2.3	<0.1	2,3	0.60	28	52	<0.1	3.5
Ivanpah	NaN	NaN	NaN	NaN	NaN	NaN	NaN	NaN	NaN
Mesquite	10±6.1	4.8±6.8	9.4±9.9	<0.1	0.19±0.27	10±14	15±21	47±60	3.7±1.5

- 1231
- 1232
- 1233
- 1234
- 1235
- 1236
- 1237
- 1238
- 1239
- 1240
- 1241
- 1242
- 1243
- 1244
- 1245
- 1246
- 1247
- 1248
- 1249
- 1250
- 1251
- 1252
- 1253
- 1254
- 1255
- 1256
- 1257

1258

1259 Table 3. Fe content in wt % for total Fe (FeT) content, and in % for ascorbate Fe (FeA), dithionite (FeD),
1260 oxalate Fe (FeM) and structural Fe (FeS). NaN not a number.

	FeT	FeA %	FeD %	FeM %	FeS %
CRUSTS	3.0±1.3	1.8±0.92	17±7.2	2.1±1.2	79±8.5
Soda	3.1±1.2	1.5±0.81	14±2.5	1.5±0.49	83±2.8
Cronese	3.7±1.2	2.4±0.99	21±11	2.3±1.1	74±13
Coyote	3.5	1.8	14	2.4	82
Ivanpah	4.9	1.4	29	0.82	68
Mesquite	1.6±0.53	1.8±0.93	20±2.7	3.7±1.2	74±3.5
RIPPLES	1.9±1.1	1.4±1.2	12±5.6	2.4±1.8	84±7.5
Soda	2.0±1.2	0.98±0.39	10±3.4	2.1±1.8	87±4.4
Cronese	2.3±1.5	1.4±0.35	14±9.3	2.8±2.9	82±12
Coyote	1.3	3.4	26	3.0	68
Ivanpah	NaN	NaN	NaN	NaN	NaN
Mesquite	1.0±1.1	3.6±3.0	20±1.2	4.4±1.2	73±4.1

1261

1262

1263

1264

1265

1266

1267

1268

1269

1270

1271

1272

1273

1274

1275

1276

1277

1278

1279

1280

1281

1282

1283

1284

1285

1286

1287

1288 Table 4. Summarise MDPSD (μm), FDPSD (μm) median particle diameter, Quartz (Qtz, wt %), feldspars
 1289 (Feld., wt %), clay mineral (Clay, wt %), carbonates (Carb., wt %), Na-salts (Na-S, wt %), Gypsum (Gp,
 1290 wt %), total Fe content (FeT, wt %), exchangeable Fe (FeA, wt %), dithionite Fe (Hematite and Goethite,
 1291 wt %), oxalate Fe (FeM, wt %) and structural Fe (FeS, wt %) for Mojave and Morocco crusts and Iceland
 1292 top sediments. NaN not a number.
 1293

	MDPSD d(0.5)	FDPSD d(0.5)	Qtz	Feld.	Clay	Carb.	Na-S	Gp	FeT	FeA	FeD	FeM	FeS
Mojave	92	37	16	37	24	6.6	7.3	3.1	3.0	0.06	0.53	0.06	2.4
Morocco	113	37	48	9.4	17	22	7.0	0.64	3.6	0.07	1.1	NaN	2.4
Iceland	55	56	0.21	20	NaN	NaN	NaN	NaN	9.3	0.15	0.43	1.4	7.3

1294
 1295
 1296